A long-term high-resolution air quality reanalysis with public facing air quality dashboard over the Contiguous United States (CONUS)

Rajesh Kumar[1], Piyush Bhardwaj[1,*], Cenlin He[1], Jennifer Boehnert[1], Forrest Lacey[1], Stefano Alessandrini[1], Kevin Sampson[1], Matthew Casali[1], Scott Swerdlin[1], Olga Wilhelmi[1], Gabriele G. Pfister[1], Benjamin Gaubert[1], and Helen Worden[1]

[1]NSF National Center for Atmospheric Research, Boulder, CO, USA

*Now at Center for Study of Science, Technology and Policy (CSTEP), Bengaluru, India

Corresponding author: Rajesh Kumar (rkumar@ucar.edu)

Keywords: Chemical data assimilation, WRF-CMAQ, GSI, Air Quality Dashboard

Abstract

We present a 14-year 12-km hourly air quality dataset created by assimilating satellite observations of aerosol optical depth (AOD) and carbon monoxide (CO) in an air quality model to fill gaps in the contiguous United States (CONUS) air quality monitoring network and help air quality managers understand long-term changes in county level air quality. Specifically, we assimilate the Moderate Resolution Imaging Spectroradiometer (MODIS) AOD and the Measurement of Pollution in the Troposphere (MOPITT) CO observations in the Community Multiscale Air Quality Model (CMAQ) every day from 01 Jan 2005 to 31 Dec 2018 to produce this dataset. The Weather Research and Forecasting (WRF) model simulated meteorological fields are used to drive CMAQ offline and to generate meteorology dependent anthropogenic emissions. Both the weather and air quality (surface fine particulate matter ($PM_{2.5}$) and ozone) simulations are subjected to a comprehensive evaluation against multi-platform observations to establish the credibility of our dataset and characterize its uncertainties. We show that our dataset captures regional hourly, seasonal, and interannual variability in meteorology very well across the CONUS. The correlation coefficient between the observed and simulated surface ozone and $PM_{2.5}$ concentrations for different Environmental Protection Agency (EPA) defined regions across CONUS are 0.77-0.91 and 0.49-0.79, respectively. The mean bias and root mean squared error for modeled ozone are 3.7-6.8 ppbv and 7-9 ppbv, respectively, while the corresponding values for $PM_{2.5}$ are -0.9-5.6 $\mu g/m^3$ and 3.0-8.3 $\mu g/m^3$, respectively. We estimate that annual CONUS averaged maximum daily 8-hour average (MDA8) ozone and $PM_{2.5}$ trends are -0.30 ppb/year and -0.24 $\mu g/m^3$/year, respectively. Wintertime MDA8 ozone shows an increasing but statistically insignificant trend at several sites. We also found a decreasing trend in the 95th percentile of MDA8 ozone but an increasing trend in the 5th percentile. Most of the sites in the Pacific Northwest show an increasing

but statistically insignificant trend during summer. An ArcGIS air quality dashboard has been developed to enable easy visualization and interpretation of county level air quality measures and trends by stakeholders, and a Python-based Streamlit application has been developed to allow the download of the air quality data in simplified text and graphic formats.

1. Introduction

Air quality is one of the most important global environmental concerns as almost the entire global population (99%) is estimated to breathe air that exceeds the World Health Organization (WHO) defined Air Quality Guidelines (WHO, 2023). Exposure to ambient air pollution causes about 4.2 million premature mortalities every year (WHO, 2020). Air quality has improved substantially over the past two decades in the US as the Environmental Protection Agency (EPA) observations show that maximum daily 8h average (MDA8) surface ozone levels have decreased by 29% over 1980-2021, and annual average concentrations of particulate matter with an aerodynamic diameter smaller than 2.5 μm ($PM_{2.5}$) have decreased by 37% over 2000-2021 (https://www.epa.gov/air-trends/air-quality-national-summary). However, air pollution continues to violate the National Ambient Air Quality Standards (NAAQS) in many parts of the US, such as the Colorado Front Range, California, northeast US, and nearly all the national parks. A recent study reported that 97% of US national parks suffer from significant or unsatisfactory levels of harm from air pollution (Orozco et al., 2024). Poor air quality is reported to cause about 160,000 premature deaths in the US, with a total economic loss of about $175 billion (Im et al., 2018). Exposure to air pollution levels even below the EPA NAAQS can adversely affect human health (Di et al., 2017). To mitigate the risks of air pollution and how air quality is responding to emission control policies, it is, therefore, imperative to quantify past changes in air quality.

Numerous studies have revealed several key features of long-term changes in surface ozone and $PM_{2.5}$ over the US using long-term observations from the EPA monitoring networks. First, both the urban and rural sites in the eastern US show negative ozone trends during the summer season (Butler et al., 2011; Cooper et al., 2012), but lower ozone levels at some sites have an increasing trend during winter and early spring (Bloomer et al., 2010; Cooper et al., 2012; Simon

et al., 2015). Second, surface and free tropospheric ozone show positive trends in all seasons at rural and remote sites in the western US (Jaffe and Ray, 2007; Cooper et al., 2012). Third, increasing ozone is observed in the inflow to the US west coast (Jaffe et al., 2003), over the North Pacific (Parrish et al., 2004), and west coast marine boundary layer (Parrish et al., 2009). The Tropospheric Ozone Assessment Report (TOAR) showed that summertime surface ozone continues to decrease over the US, but the trend is less certain at the urban sites (Chang et al., 2017; Fleming et al., 2018). Similar regional and seasonal differences in the long-term trends are also seen in $PM_{2.5}$ and its components. For example, carbonaceous aerosols (organic and black carbon) show a widespread decrease over 1990-2010 across the US in winter and spring and show positive but insignificant trends over the western US (Hand et al., 2013). $PM_{2.5}$ levels continue to decrease over the majority of the US except in the wildfire-prone areas (McClure and Jaffe, 2018).

In addition to the observation-based trend analysis, chemical transport model (CTM) simulations have been employed to interpret the observed trends. For example, the increase in lower ozone values can be attributed to the increase in Asian emissions from 1980-1995 (Fiore et al., 2002). The anthropogenic emissions and natural variability were found to have competing effects on surface ozone over much of the US over 1980-2005 (Pozzoli et al., 2011). Another study reproduced negative summertime ozone trends over the eastern US but underestimated the positive trends in the western US likely due to underestimation of Asian emission trends or trans-pacific transport or changes in stratosphere-troposphere exchange (Koumoutsaris and Bey, 2012). Lin et al. (2017) quantified the contributions of rising Asian emissions, domestic U.S. emission controls, wildfires and climate to changes in surface ozone from 1980 to 2014. Several studies have also quantified the contributions of wildfires to $PM_{2.5}$ trends in the U.S. (Xie et al., 2020, Burke et al., 2023). While global models captured most of the observed variability and trends in summertime

Formatted: Subscript

ozone, the use of high-resolution regional models is recommended to reproduce interannual variability in winter and spring in the western US (Strode et al., 2015).

Apart from the interpretation of observed trends, the CTMs also provide information in areas with no observations. However, CTM simulations suffer from both systematic (i.e., biases) and random errors due to a number of factors, including numerical approximations, inadequate understanding of some processes that control the spatial and temporal distribution of air pollutants, inaccuracies in the initialization of the physical and chemical atmospheric state, and uncertainties in the emission inventories. While continuous efforts are being made to improve the representation of processes controlling $PM_{2.5}$ and ozone (Appel et al., 2010, 2013, 2017; Nolte et al., 2015; Fahey et al., 2017) and emission inventories are updated by the EPA every three years, recent developments have shown that assimilation of the National Aeronautics and Space Administration (NASA) satellite retrievals of atmospheric composition in CTMs can significantly improve air quality simulations (Gaubert et al., 2016; Kumar et al., 2019; Liu et al., 2011; Pagowski et al., 2014; Saide et al., 2013). NASA satellite retrievals of atmospheric constituents with a far greater spatial coverage compared to ground-based monitoring networks presents a unique opportunity to develop long-term high-resolution air quality reanalysis, which can be useful for quantifying air quality changes in unmonitored areas and assessing the impacts of changes in air quality on human health and ecosystems.

This paper describes the methodology and evaluation of a long-term high-resolution regional air quality reanalysis generated over the CONUS from 2005 to 2018 by assimilating the Moderate Resolution Imaging Spectroradiometer (MODIS) aerosol optical depth (AOD) and the Measurement of Pollution in the Troposphere (MOPITT) carbon monoxide (CO) retrievals daily in the Community Multiscale Air Quality (CMAQ) model. Our regional reanalysis is based on

three-dimensional variational (3DVAR) approach, which is different compared to the four-dimensional variational (4D-Var) approach (Innes et al., 2019) and Ensemble Kalman Filter approaches (Gaubert et al. 2017, Miyazaki et al., 2020, Kong et al., 2021) used in recent long-term global and regional air quality reanalysis. Among these, 3DVAR is computationally the most efficient approach because it uses only a single model simulation, but its accuracy can be limited by the assumption of a constant background error covariance matrix that both 4DVAR and EnKF address. An air quality dashboard developed to enable the use of this dataset by a variety of stakeholders is also described.

2. Methodology

2.1. The Chemical Transport Model

The CMAQ model version 5.3.2 driven offline by the Weather Research and Forecasting (WRF) model version 4.1 is used to simulate air quality over the CONUS from 01 Jan 2005 to 31 Dec 2018. We employ the "cb6r3_ae7_aq" chemical mechanism that uses Carbon Bond 6 version r3 for gas-phase chemistry and AERO7 aerosol module for representing aerosol processes, including secondary organic aerosols (Appel et al., 2021). Both the WRF and CMAQ models use a horizontal grid spacing of 12 x 12 km^2 with WRF (CMAQ) grid using 481 (442), 369 (265), 36 (35) grid points in the longitudinal, latitudinal, and vertical directions, respectively. The model top is set to 50 hPa for both the models. The meteorological initial and boundary conditions for WRF are based on the six hourly ERA-Interim analyses at a grid spacing of 0.7^o x 0.7^o. We follow Appel et al. (2017) for physical parameterizations, four-dimensional data assimilation, and soil moisture nudging settings in WRF.

Emissions from several anthropogenic emissions sectors such as residential wood combustion, agricultural emissions from livestock and fertilizer applications, and mobile sources depend on meteorological conditions. For example, ambient temperature affects the heating demand, affects the volatilization of emissions from fertilizer use, drives air conditioning use, etc. The SMOKE modeling system allows us to simulate these relationships. To be consistent in the use of meteorological fields for both emission processing and driving CMAQ, we generate meteorology-dependent anthropogenic emissions for the EPA National Emissions Inventory (NEI) base years of 2011, 2014, and 2017 by feeding the WRF meteorological fields to the Sparse Matrix Operator Kernel Emissions (SMOKE). The emissions for 2005-2010 are derived by applying EPA reported annual state-wise trends to the NEIv2 2011 emissions. While NEI emissions are available for 2005 and 2008, the emissions processing platform for 2005 and 2008 does not process emissions for the "cb6r3_ae7_aq" chemical mechanism of CMAQ used here. Similarly, NEIv2 2014 emissions are used to derive emissions for 2012 and 2013, and the NEIv1 2017 emissions are used to derive anthropogenic emissions for the rest of the years. Fire emissions in CMAQ are represented using the Fire Inventory from NCAR (FINN) version 2.2 which provides daily varying global fire emissions at 1 x 1 km^2 resolution (Wiedinmyer et al., 2023). FINN emissions are processed through SMOKE to enable inline plume rise of fire emissions within CMAQ. Biogenic emissions are calculated online within the model using the Biogenic Emission Inventory System (BEIS). The chemical boundary conditions are based on 6-hourly Whole Atmosphere Community Climate Model (WACCM) simulations (Marsh et al., 2013; Gettelman et al., 2019). The WACCM output is mapped onto CMAQ grids using the Initial Conditions Processor (ICON) and Boundary Conditions Processor (BCON).

Deleted: W

2.2. Data Assimilation System

We have used the three-dimensional variational (3DVAR) capability of the community Gridpoint Statistical Interpolation (GSI) version 3.5 to assimilate the Level 2 MODIS AOD retrievals and the Level 2 MOPITT CO retrievals in CMAQ. The MODIS AOD assimilation framework is the same as we developed previously (Kumar et al., 2019) and the MOPITT CO assimilation capability has been developed in this work. We use total aerosol mass per mode (Aiken, Accumulation, and Coarse) and CO mixing ratios as the control variables in GSI. The state variables include individual aerosol components, total aerosol mass per mode, CO mixing ratios, meteorological variables (temperature, pressure, and relative humidity), and CMAQ vertical grid. Daily MODIS and MOPITT retrievals are converted into a format compatible with GSI input modules.

A climatological background error covariance (BEC) matrix is generated separately for winter (January) and summer (July) conditions using the GEN_BE tool, which reads two different WRF-CMAQ runs driven by different meteorological and emission inputs but valid at the satellite overpass time. Since there are multiple overpasses of the Terra and Aqua satellites that host the MOPITT and MODIS sensors, we calculate the BEC at 15 Z, 18 Z, and 21 Z. The winter BEC is used when assimilating satellite retrievals from November through March and the summer BEC is used for the rest of the months. Our BEC design considers the uncertainties in meteorology, anthropogenic, and biomass burning emissions. Meteorological uncertainties are represented by using two different sets of physical parameterizations (Table A3.1) in two WRF runs to capture errors in meteorology related to assumptions used in physical parameterizations. Species-dependent perturbation factors for anthropogenic and biomass burning emissions are estimated by comparing a number of available global/regional anthropogenic and biomass burning emission inventories over the CONUS (Table A3.2 and A3.3). Among the two WRF-CMAQ runs fed to

GEN_BE for BEC estimation, we used the default emissions in the first run and perturbed the emissions in the second run. The BEC was then estimated in terms of variances and length scales (both horizontal and vertical) for total aerosol mass per mode and CO, and used in GSI. We refer the reader to Kumar et al. (2019) for a description of BEC parameters.

We have assimilated standard Level 2 Collection 6.1 MODIS AOD and Version 8 MOPITT CO retrievals based on the multispectral algorithm (thermal and near infrared) in CMAQ. This multispectral product is more sensitive to near-surface CO over land compared to the thermal-infrared only retrievals. MOPITT retrievals agree with in-situ measurements at all vertical levels within ±5% (Deeter et al., 2019). The observation errors for MODIS AOD retrievals are specified as (0.03 + 0.05 * AOD) and (0.05 + 0.15 * AOD) over the ocean and the land, respectively (Remer et al., 2005). The observation errors for CO profiles are used as reported in the MOPITT retrieval product. A simple forward operator and its adjoint based on the parameterization of (Malm and Hand, 2007) is used to convert CMAQ aerosol chemical composition into AOD for a direct comparison with MODIS AOD retrievals as described in Kumar et al. (2019). The forward operator and its adjoint for MOPITT CO assimilation are developed in this study and described in Appendix A1.

2.3. Reanalysis production workflow

Daily analyses of three-dimensional fields of aerosols and CO based on the assimilation of MODIS AOD and MOPITT CO retrievals in CMAQ using the GSI system has been performed using the workflow shown in Figure 1. The first CMAQ simulation on 01 Jan 2005 is initialized using the global model simulations from WACCM, and all subsequent simulations until 31 Dec 2018 are initialized from the previous CMAQ simulations. Every day, we perform 9 simulations following

the availability of new satellite observations every three hours owing to difference between Terra and Aqua overpass times. The first simulation runs CMAQ from 00-15 Z, the second simulation assimilates MODIS Terra and Aqua AOD retrievals at 15 Z, and third simulation assimilates MOPITT CO retrievals at 15 Z. The fourth simulation advances CMAQ from 15 Z to 18 Z with the fifth and sixth simulations assimilating MODIS AOD and MOPITT CO at 18Z, respectively. The seventh simulation advances CMAQ from 18 Z to 21 Z, the eighth simulation assimilates MODIS Aqua AOD retrievals at 21 Z, and the ninth simulation advances CMAQ from 21 Z to 00 Z of the next day. This resulted in a total of 46,152 jobs submission on the NCAR supercomputer Cheyenne (https://arc.ucar.edu/knowledge_base/70549542). An automated script was developed to submit and track successful completion of these jobs.

The assimilation times of 15 Z, 18 Z, and 21 Z were determined based on the analysis of overpass times of Terra and Aqua satellites, which pass over the CONUS between 13:30 Z and 22:30 Z. All the satellite retrievals belonging to a 3-hour window are assumed to be available for assimilation at the center of that window. For example, all the satellite retrievals between 1330 Z and 1630 Z are assimilated at 1500 Z.

Our previous work has shown that the assimilation of MODIS AOD in CMAQ improved the correlation coefficient between CMAQ simulated and independently observed $PM_{2.5}$ by ~67% and reduced the mean bias by ~38% over the CONUS during July 2014. To understand whether GSI pushes CMAQ towards MOPITT, we performed and compared one month (July 2018) of CMAQ experiments with and without assimilation of MOPITT CO profiles. We find that the assimilation of MOPITT CO profiles substantially improves the correlation coefficient and reduces the errors (both mean bias and root mean squared error) between CMAQ and MOPITT CO at all the pressure levels except at 100 hPa where the MOPITT sensitivity is the lowest (Appendix A2,

Deleted: ,
Deleted: with t
Deleted: running
Deleted: assimilating
Deleted: assimilating

Figure A2.1). This simple test confirms the ability of GSI to constrain the performance of CMAQ with satellite observations. Other trace gas species (e.g., ozone and OH) are not affected directly by the assimilation of AOD and CO, but the impact of assimilation indirectly affects these species through photochemical processes in the model. For example, we found instantaneous changes in surface ozone in the range of -1.3 to 3.2 ppbv but monthly average changes are within the range of ±0.3 ppbv during July 2018.

2.4. Output frequency and optimization

The production of a chemical reanalysis also poses a challenge of storing the model output. Since our chemical reanalysis focuses on air quality applications, we saved all the chemical variables together with relevant meteorological parameters (2 m temperature and relative humidity, 10 m wind speed and direction, planetary boundary layer height, precipitation, and downward reaching solar radiation) and deposition (both dry and wet) fluxes every hour at the surface. The total size of this output is 12 Terabytes.

3. Ground-based observations and trend calculation method

We have obtained and processed hourly in-situ measurements of 2 m temperature (T2), 2 m relative humidity (RH), 10 m wind speed (WS10), 10 m wind direction (WD10), and surface pressure from the METeorological Aerodrome Reports (METAR) network, which is distributed by the NCEP's Meteorological Assimilation Data Ingest System (MADIS). METAR data are surface weather observations and it consists of meteorological data from airports (Automated Surface Observing Systems) and other permanent weather stations (Automated Weather Observing System) located throughout the US. We used the Level-3 Quality Controlled METRAR data over CONUS to

Deleted: 2

evaluate our modeled meteorological fields (https://madis.ncep.noaa.gov/madis_metar.shtml). Daily precipitation data from the 0.1-deg Integrated Multi-satellitE Retrievals for Global precipitation measurements (IMERG; https://gpm.nasa.gov/data/imerg) dataset is used to evaluate WRF simulated precipitation.

To evaluate the modeled surface $PM_{2.5}$ and ozone concentrations, we have obtained hourly $PM_{2.5}$ and ozone observations from the EPA Air Quality System, which currently measures $PM_{2.5}$ and ozone at more than 1000 sites across the US. The AQS data also contains values below the method detection limit (MDL). The MDLs are different for ozone and $PM_{2.5}$ and also vary as a function of site and instrument type. For consistency, we assume the MDL values of 5 ppb for ozone and 2 $\mu g/m^3$ for $PM_{2.5}$ for all sites. All the data below MDL was replaced by MDL/2 (https://www3.epa.gov/ttnamti1/files/ambient/airtox/workbook/AirtoxWkbk4Preparingdataforanalysis.pdf; https://pubs.acs.org/doi/10.1021/es071301c). The sites for which two simultaneous measurements (corresponding to two instruments) were available, the mean value is taken for further calculation.

The trend calculations were performed using both the observed and modeled ozone and $PM_{2.5}$ values. The monthly mean time series of observed and modeled maximum daily 8-hour (MDA8) ozone and 24-hour average $PM_{2.5}$ during 2005-2018 is calculated over all measurement sites. The daily MDA8 ozone over a site is calculated using the EPA's defined methodology (https://www.govinfo.gov/content/pkg/FR-2015-10-26/pdf/2015-26594.pdf, pp 168). For each day, 8-hour running averages are taken from 7 am to 11 pm local standard time, which constitutes 17 8-hour running mean values per day. If an 8-hour window has less than 6 hours of data and the mean value of the remaining hours is less than 70 ppb then the data for that window is discarded. If a site has fewer than 13 valid 8-hour mean values or the maximum value of the available 8-hour

282 average is less than 70 ppb then the value for that day is discarded. For $PM_{2.5}$, a daily 24-hour
283 average value is calculated in local standard time only if at least 18 hours of valid data/day are
284 available. Furthermore, we discarded all sites with (1) < 50% data per month, (2) < 50 % data
285 during each year, and (3) if number of years with ≥ 50% data were < 10 years during 2005-2018.
286 The number of valid sites fulfilling the above criteria over CONUS are estimated to be 1012 and
287 369, for MDA8 ozone and 24-hour $PM_{2.5}$, respectively. Daily values of MDA8 ozone and 24-hour
288 $PM_{2.5}$ are used to calculate monthly 5th percentile, 50th percentile, 95th percentile and mean time
289 series during 2005-18 at each valid site. A similar criterion for seasonal mean, 5th, 50th and 95th
290 percentile time series was also used. The number of valid sites during summer season were the
291 maximum (1010/357 for MDA8 O_3/24-hour $PM_{2.5}$) and were minimum (501/337 for MDA8
292 O_3/24-hour $PM_{2.5}$) during the winter season. These annual and seasonal MDA8 ozone and $PM_{2.5}$
293 time series are then used to estimate annual and seasonal trends and the significance of trend values
294 are also tested.
295
296 **4. Results and Discussions**
297 **4.1. Meteorological evaluation**
298 The WRF simulations for the entire period (2005-2018) processed using the Meteorology-
299 Chemistry Interface Processor (MCIP) are collocated with METAR observations of T2, RH,
300 WS10, and WD10 in space and time, and paired values are used for evaluating the model. The
301 evaluation is performed at a regional scale following the EPA regional classification of the
302 CONUS in 10 regions (see Appendix A2, Figure A2.2). The number of METAR sites during 2005-
303 2018 was 1290, and the maximum available hourly data during the study period was 33-68 % over
304 10 EPA regions. Region 8 has the least data (~33-37%), and other regions have 47-68 % data

Deleted: RH2

during 2005-2018. Monthly regional averaged model and METAR observations time series are compared over 10 EPA regions for T2 (Figure 2), RH (Figure 3), WS10 (Figure 4), and WD10 (Figure 5). Three statistical metrics, namely correlation coefficient (r), mean bias (MB), and root mean square error (RMSE), for each region are also listed in Figures 2-5.

Monthly regional averaged T2 between model and observations (Figure 2) show excellent correlations of 0.8-1.0 with low mean biases of -0.3 to 0.4 ºC and the RMSE ranging from 2.0-5.7 ºC over the 10 EPA regions. The model also performed well (r = 0.7-0.9) in simulating RH (Figure 3) over 10 EPA regions with the mean biases of 0.9-3.6 % and the RMSE of 12.5 - 16.3 %. Since RH is estimated as a ratio of vapor pressure to saturation pressure (es) and es depends on T2, the biases in T2 also contribute to the biases in RH. For example, EPA Region 6 which shows the highest T2 RMSE also shows the highest RH RMSE. The model reproduces the variations in surface pressure very well (r = 1.0) with a slight underestimation (MB = -8.1 to 0.2 hPa; RMSE = 0.3-8.1 hPa). The slight underestimation in pressure is seen in eight out of 10 EPA regions with the largest MB in Regions 9 (-8.1 hPa) and 10 (-7.4 hPa). The errors in surface pressure (plot not shown) over these regions could also contribute to biases in T2 and RH.

Prior to 10 m wind speed comparison, model wind speeds are assigned "zero value" if the hourly wind speed at any site is less than 0.51 m/s (1 knot). This step was needed to make model output consistent with the METAR wind speed data, which treats such wind speeds as calm winds and assigns it a zero value. Our model simulation slightly overestimates (MB = 0.1-0.8 m/s) WS10 (Figure 4) over most of EPA regions with the exception of Region 8 (MB = -0.1 m/s). Wind direction (Figure 5) biases (absolute) over these regions were 34º-58º. The correlation coefficients for both WS10 and WD10 are slightly lower in Regions 8-10, which is likely due to the complex topography in these regions. The correlation coefficients for 10 m wind speed were lower than

Deleted: Hourly
Deleted: RH2
Deleted: Hourly
Deleted: RH2
Deleted: .
Deleted: RH2
Deleted: RH2
Deleted: RH2
Deleted: RH2

those for temperature, and relative humidity, indicating a slightly poorer model performance for winds. The WRF model is known to overpredict 10 m wind speed at low to moderate wind speeds in all available planetary boundary layer (PBL) schemes (Mass and Ovens, 2010). This shortcoming of the model was partly attributed to unresolved topographical features by the default surface drag parameterization, which in turn influences surface drag and friction velocity, and partly to the use of coarse horizontal and vertical resolutions of the domain (Cheng et al., 2005). The WRF model also captures the seasonally averaged diurnal variations in T2, RH, and 10 m Wind speed very well but overestimates the wind speed particularly at night (see Appendix A2, Figure A2.3).

Since WRF and IMERG precipitation have different resolutions, we first mapped the WRF simulated precipitation from a 12 km x 12 km grid on Lambert conformal projection to the IMERG rectilinear grid of 0.1° x 0.1° using the "rcm2rgrid" functionality of the NCAR command language (https://www.ncl.ucar.edu/Document/Functions/Built-in/rcm2rgrid.shtml). The seasonal mean WRF simulated and IMERG derived precipitation are then compared over four seasons during 2005-2018 (Figure 6). The model is able to capture the spatial patterns in precipitation in different seasons, with an underestimation of -0.1 to -0.9 mm/day. The highest underestimation is observed during the winter season. The eastern CONUS showed an underestimation during winter, spring and autumn seasons, however, over the western US, the model mostly overestimated the precipitation, especially in the mountainous regions (Rockies, Cascades, and Sierra Nevada). The model also showed larger biases over the lakes and oceanic regions. Despite the biases, this comprehensive evaluation shows that our model simulations captured the key features of regional and temporal variability of the key meteorological parameters over the CONUS fairly well.

4.2. Air Quality evaluation

Hourly regional averaged observed and CMAQ simulated surface ozone and $PM_{2.5}$ are compared for all the EPA regions in Figures 7 and 8, respectively. In all the regions, the model captures the seasonal cycle in surface ozone characterized by a summertime peak as well as the observed interannual variability very well, with correlation coefficients of 0.77 to 0.91. The model also overestimates the nighttime ozone levels in all the regions (see Appendix A2, Figure A2.4), but a larger overestimation is seen in Regions 8 and 9. The mean bias and RMSE in modeled ozone are very similar across the regions, with values ranging from 3.7 - 6.8 ppbv and 7.0-9.0 ppbv, respectively. The model shows a slightly poorer skill in capturing the variability in $PM_{2.5}$ relative to ozone as reflected by smaller r values of 0.49-0.79 but captures long-term trends in most of the regions reasonably well. The mean bias and RMSE in modeled $PM_{2.5}$ are estimated to be -0.9 to 5.6 $\mu g/m^3$ and 3.0 to 8.3 $\mu g/m^3$, respectively. The largest underestimation of $PM_{2.5}$ is seen in Region 8, particularly from 2005 to 2012 while the largest overestimation is seen in Region 2.

In addition to regional evaluation, we also evaluated the model performance for different land use types and location settings (see Appendix A2, Figure A2.5 for classification of the number of sites in these categories). This categorization information by land use and location types was not available for a very small number of sites, and thus, they were excluded from the analysis (sites classified as "NONE" in Figure A2.2). Since Maximum Daily Averaged 8-hour (MDA8) ozone and daily averaged $PM_{2.5}$ are policy-relevant metrics, we focus on the evaluation of these parameters on a monthly averaged scale for this evaluation. We evaluate monthly median (50^{th} percentile), 5^{th} and 95^{th} percentile time series of MDA8 ozone, and daily averaged $PM_{2.5}$ for different land use categories and location settings (Appendix A2, Figures A2.6-A2.11).

Deleted: 2

Deleted: 3

Deleted: 8

Among the rural sites, all land use categories showed the highest biases for the 5th percentile, followed by the median and 95th percentile for MDA8 ozone, except for the "Others" category, for which the median showed the lowest bias. For suburban and urban site types, 95th percentile MDA8 ozone consistently showed the lowest bias for all land use types, followed by the median and 5th percentile. Furthermore, "Others" land use category under the rural and urban sites shows the lowest bias for 5th percentile and the median, while "residential" land use type shows the lowest bias for the suburban sites.

For $PM_{2.5}$, the largest differences between the model and observations are seen for the 95th percentile at "Others" land use categories compared to the 5th percentile and median. The model generally captures the temporal variability in $PM_{2.5}$ across all land use types (except "Others") and location settings for all three-percentile metrics analyzed here but some anomalies are also evident. For example, residential and commercial sites in the urban category show larger overestimation for the median and 95th percentiles during 2005-2006, indicating higher uncertainties in anthropogenic emission estimates at these sites during these years. While the model follows most of the observed peaks in 95th percentile, it substantially underestimates the observed peaks.

The errors in air quality simulations can be attributed to the uncertainties in different types of emissions used to drive air quality models, errors in the lateral boundary conditions representing pollution inflow, uncertainties in meteorological parameters (as quantified earlier in this section), and poor understanding of some of the physical and chemical processes controlling the fate of those emissions. To quantify uncertainties in anthropogenic and biomass burning emissions over the CONUS, we compared all available anthropogenic and biomass burning emission inventories over the CONUS and found that anthropogenic emission estimates across various emission inventories vary by a factor of 1.16 - 2.94 (Table A3.2) and the corresponding fire emission

estimates vary by 3.13 - 8.0 (Table A3.3). The extrapolation of the NEI emissions to years other than the base years might have also introduced some uncertainties in our simulations because EPA reported state level trends may not always represent local (sub-state) changes in emissions and also do not provide information about new emission sources appearing in the CONUS between two NEI base emission inventory years. In addition, the observation error (0.05 + 15% of MODIS AOD value over land; Remer et al., 2005) for MODIS AOD increases with increase in the magnitude AOD which in turn restricts the data assimilation system (GSI) in pushing the modeled AOD towards the MODIS AOD. Furthermore, the AOD retrievals do not contain any information about the vertical distribution of aerosols and thus GSI simply scales the modeled vertical profile to match the MODIS AOD within the constraints of observation and model error. Thus, AOD assimilation is unable to correct for any errors in vertical distribution of aerosols resulting from errors in the plume rise of fire emissions.

4.3. Trend analysis

To help air quality managers and the public determine the confidence they can put in using this reanalysis for analyzing changes in air quality in their regions, we have evaluated the trends in our CMAQ simulated MDA8 ozone and 24-hr average $PM_{2.5}$ against the AQS observations. The spatial distribution of positive/negative trend values in MDA8 ozone and 24-hr average $PM_{2.5}$ calculated using monthly median values in AQS and CMAQ data during 2005-2018 are shown in Figures 9 and 10, respectively. Different symbols are used to represent urban, suburban, and rural site types. Based on location, ~42/23% of sites were in rural areas, ~41/45 % in suburban areas and ~17/32% were in urban or city centers, respectively, for MDA8 ozone/24-hr average $PM_{2.5}$. Darker/lighter red and blue colors represent statistically significant/insignificant increasing and

Formatted: Subscript

decreasing trends at 2-sigma level. The 2-sigma rule is a standard way of testing statistical significance of trends. In a normal distribution, ~95% of the data points lie within 2 standard deviations (±2-sigma) of the mean. If the trend falls outside this range, it is considered unlikely to have occurred by chance (i.e., at a statistical significance in the probability of less than 5%). Over the study period, both the model and observations show decreasing trends in MDA8 ozone over the majority of the CONUS. Most eastern US sites show decreasing trends that were statistically significant with p values less than 0.05. The sites located in western/northwestern US, however, showed mixed results with some sites showing increasing trends, most of which were not statistically significant. Similar results were observed during the summer season with most sites showing statistically significant decreasing trends over the most locations. During autumn and winter seasons, several sites over California and the eastern US showed decreasing but insignificant trends. Some sites over the midwestern US also changed the trend sign during these seasons. The trends in winter seasons were mostly positive over most sites in the US (except for the coastal sites in the southeastern US). About 55% (278 of 501) of the sites showed positive trends in both AQS and CMAQ data during winter but only ~3% (29 of 1012) of the sites showed positive trends in summer. The seasonal changes in monthly median trends discussed above were mostly consistent (67-86%) between the AQS and CMAQ data. A similar analysis with 5th and 95th percentile time series suggested that the higher percentiles showed mostly decreasing trends, but 5th percentile dataset at the mid-western US, Boston-New York-DC, and central US sites showed increasing trends on a seasonal and annual basis. The MDA8 ozone trend over CONUS (1012 sites) is estimated to be -0.53 ± 0.46/-0.56 ± 0.45 ppb/year (summertime) and -0.31 ± 0.43/-0.29 ± 0.39 ppb/year (annual), respectively, for AQS/CMAQ data, with most sites (~70 %) showing negative trends. At the 2-sigma level (p-value < 0.05), the summertime mean ozone trends

Deleted: (increasing, 55% agreement between AQS and CMAQ)…

Deleted: The number of sites with negative trend values in summer changed from 3% to 55% positive trends during winter season.…

Deleted: Most of these trends, however, were not statistically significant and the number of sites was also reduced to about 560% of the sites available for annual evaluation during this season.

464 are -0.85± 0.36/-0.75 ± 0.35 ppb/year for 484/620 sites and annual MDA8 ozone trends are -0.52
465 ± 0.45/-0.47 ± 0.42 ppb/year for 554/562 sites, respectively, for AQS/CMAQ data over CONUS.
466 This suggests decreases in monthly high ozone days but increases in monthly low ozone. On an
467 annual basis, MDA8 ozone showed the most decreasing trends (AQS/CMAQ= -0.40 ± 0.37/-0.34
468 ± 0.34 ppb/year) in the 428 rural sites. The mean ozone trends over urban (411 sites) and suburban
469 (170) areas were (AQS/CMAQ = -0.28 ± 0.44/-0.29 ± 0.40 ppb/year) and (AQS/CMAQ = -0.13 ±
470 0.48/-0.15 ± 0.48 ppb/year), respectively. The ozone trends over high-altitude sites (16 sites), are
471 mostly negative for AQS/CMAQ = -0.43 ± 0.45/-0.12 ± 0.36 ppb/year) in summer and annually
472 (AQS/CMAQ, = -0.39 ± 0.38/-0.03 ± 0.29 ppb/year).

473 Similar MDA8 ozone trends were also reported in a previous study (Simon et al., 2015).
474 Mousavinezhad et al. (2023) reported that all regions except the Northern Rockies and the
475 Southwest experienced decreasing trends in median MDA8 ozone values during the warm season
476 of 1991-2020, with rural stations in the Southeast and urban stations in the Northeast experiencing
477 the greatest declines of -1.29 ± 0.07 ppb/year and -0.85 ± 0.08 ppb/year, respectively. They also
478 reported a large decrease in MDA8 ozone 95th percentile in all regions. Similarities in ozone trends
479 between the AQS observations and CMAQ simulations over a longer time period 1990-2015 is
480 also reported by He et al. (2020).

481 On an annual basis, 24-hr average $PM_{2.5}$ also showed mostly decreasing trends (~79 %)
482 over most of the sites. A majority of these trends were also statistically significant at 2-sigma level
483 (AQS/CMAQ = 70 %/75 %). However, unlike MDA8 ozone, an increasing trend (though
484 insignificant) in summertime $PM_{2.5}$ is observed over the north-western US (Fig. 10). The
485 wintertime trends were also mostly decreasing over most of the sites, except for the northwestern
486 US. During summer season about 5-fold increase (annual ~ 5%; summer ~ 24%) in positive trends

Deleted: 9

is observed in high $PM_{2.5}$ days (95th percentile time series) and most of these increases were observed over the Pacific Northwest. These summertime increases in $PM_{2.5}$ trends are also evident from the 95th percentile time series, where a sharp increase in $PM_{2.5}$ is observed during 2017-2018 overall sites except industrial locations (see Figure A2.11). In recent years these changes could be even stronger as wildfire activity over the western US has increased in the last decade. The dramatic decreasing trends of $PM_{2.5}$ in the eastern US were also reported in previous studies (Zhang et al., 2018; Gan et al., 2015; Xing et al., 2015) (Gan et al., 2015; Xing et al., 2015; Zhang et al., 2018) due to emission reductions. The increasing trend in the western central area is due in part to frequent wildfires (Dennison et al., 2014; McClure and Jaffe, 2018). For $PM_{2.5}$ the overall mean trends are -0.24 ± 0.21/-0.24 ± 0.24 μg/m^3/year (369 sites) in AQS/CMAQ data sets. Unlike, MDA8 ozone, the number of sites remained almost the same (337-357 sites in four seasons, 369 annual) during seasons and an overall negative trend is also observed (-0.18 ± 0.25 to -0.30 ± 0.35 μg/m^3/year). At 2-sigma level, the number of sites that showed negative trends in both the datasets were 69-80 %.

On an annual basis, the mean $PM_{2.5}$ trends over urban sites are -0.17 ± 0.22/-0.18 ± 0.15 μg/m^3/year, suburban sites are -0.28 ± 0.22/-0.24 ± 0.26 μg/m^3/year and -0.3 μg/m^3/year, and urban and city center are -0.23 ± 0.21/-0.30 ± 0.27 μg/m^3/year μg/m^3/year, respectively, for AQS/CMAQ data. The only high-altitude site for $PM_{2.5}$ showed an increase in the annual (0.07/0.06 μg/m^3/year for AQS/CMAQ data) and summertime trend (0.13/0.13 μg/m^3/year for AQS/CAMQ data). During other seasons, mostly low negative trends were observed. The ozone trends over high-altitude sites (16 sites), however, are mostly negative (-0.43 ± 0.45/-0.12 ± 0.36 ppb/year in summer and -0.39 ± 0.38/-0.03 ± 0.29 ppb/year, annually). The ozone trends at high altitude sites

Deleted: refer to Fig.

Deleted: S8

showed large seasonal variations with min to max ranges of -0.69 to 0.87/-1.5 to 0.26 ppb/year for AQS/CMAQ data.

4.4. Air Quality dashboard

The comprehensive evaluation of our reanalysis in the above sections shows that our reanalysis is able to capture key features of long-term trends in both MDA8 ozone and $PM_{2.5}$ over most parts of the CONUS. This increases confidence in using this dataset for assessing the trends in unmonitored areas of the CONUS. Therefore, a Geographic Information System (GIS)-based dashboard has been developed to aid in community engagement and understanding of the reanalysis data. The dashboard was developed using Esri ArcGIS Dashboard technology (Esri, 2024). An interactive web-based dashboard allows stakeholders to explore air quality annual concentrations and the number of days that exceed a certain threshold over space and time. It provides a step-by-step path for users to explore information at the CONUS, state, and county levels. In the center of the dashboard is a time series chart showing trends in annual concentrations of MDA8 ozone, NO2, $PM_{2.5}$, PM_{1}, and PM_{10} between 2005 and 2018. An indicator element of a dashboard highlights how many days between 2005 and 2018 have exceeded the National Ambient Air Quality Standards (NAAQS) for ozone and $PM_{2.5}$, and a bar chart graph shows the number of days that exceeded the NAAQS each year. There is also a map that zooms to the selected state or county of interest and illustrates the spatial distribution of air quality variables using a quantitative color bar.

The dashboard can be used to better understand how particular events, such as large wildfires, have affected air quality in certain geographic areas. For example, the 2008 wildfires in Shasta and Trinity Counties in California, referred to as the June Fire Siege, had a major impact

on air quality (https://storymaps.arcgis.com/stories/c6535ee477e14b72a20393a5f10aefbc). Figure 11 shows MDA8 ozone concentrations for Shasta County, California. The dashboard shows a sharp increase in MDA8 ozone concentration in 2008, as depicted in the time series plot. The bar chart in the lower right corner also reflects the large number of days that exceeded the NAAQS criteria for MDA8 ozone in 2008.

The dashboards also can be used to visualize the efficacy of air quality management policies. For example, Los Angeles County, CA has designed and implemented strict emission standards to improve air quality. Figure 12 shows the downward trend in $PM_{2.5}$ concentrations in Los Angeles County during 2005-2018. The air quality dashboard is publicly accessible at https://ncar.maps.arcgis.com/apps/dashboards/9a97650dc77b4f7192b99ea9bef36a21. To ensure stakeholders have an understanding of the uncertainties, we have included the following message on the website: "Note that mean bias of 3.7-6.8 ppbv in ozone and that of -0.9-5.6 μg/m³ in PM2.5 could have impacted the calculation of days exceeding the corresponding National Ambient Air Quality Standards."

We have also developed a Python-based Streamlit application allowing users to select and download data for specific time periods aggregated over administrative boundaries such as cities, counties, and states. Temporal and spatial aggregations are performed on the server, and only information of interest is downloaded and delivered to the users, taking the data processing workload off of the users. The Streamlit application allows users to select a time period, a temporal aggregation (daily, weekly, monthly, annual), one or more air quality variables, statistics (min, mean, max), and an area of interest (state, county, city). The data can then be downloaded as a comma-separated file as well as graphed on the website as seen in Figure 13. The Streamlit application is available at: https://compass.rap.ucar.edu/airquality/

5. Data availability

The global meteorological datasets used to drive WRF are publicly available through National Center for Atmospheric Research (NCAR) Research Data Archive (https://rda.ucar.edu/). The SMOKE setup used to create emissions for CMAQ is accessible via EPA emissions modeling platform (https://www.epa.gov/air-emissions-modeling/emissions-modeling-platforms). FINN biomass burning emissions can be downloaded from https://rda.ucar.edu/datasets/ds312.9/. Meteorological observations used to evaluate the model performance are downloaded from https://madis-data.cprk.ncep.noaa.gov/madisPublic1/data/archive/. The EPA AQS system observations are downloaded from https://www.epa.gov/aqs. Hourly surface output from the WRF-CMAQ-GSI system can be downloaded from https://doi.org/10.5065/cfya-4g50 (Kumar and He, 2023)

Deleted: ¶
¶

6. Code availability

The WRF, CMAQ, and GSI source codes are publicly accessible at https://github.com/wrf-model/, https://github.com/USEPA/CMAQ, and https://dtcenter.org/community-code/gridpoint-statistical-interpolation-gsi/download.

7. Conclusions

Air pollution is an important health hazard affecting human health and the economy in the CONUS, yet millions of people live in counties without air quality monitors. To address this gap and help air quality managers understand long-term changes in air qualities at the county level across the CONUS, we have created a 14-year long 12-km hourly dataset by daily assimilation of

Formatted: Normal, No bullets or numbering

Deleted: Air pollution is an important health hazard affecting human health and the economy in the CONUS but still, millions of people in counties with no monitors

586 atmospheric composition observations from the NASA MODIS and MOPITT sensors aboard the
587 Terra and Aqua satellites in the Community Multiscale Air Quality (CMAQ) model from 01 Jan
588 2005 to 31 Dec 2018. The WRF model has been used to simulate meteorological parameters,
589 which are then used to drive CMAQ offline and for generating meteorology-dependent
590 anthropogenic emissions.

591 The meteorological parameters, ozone, and $PM_{2.5}$ have been extensively validated against
592 multi-platform observations to characterize uncertainties in our dataset, which air quality managers
593 need to determine the confidence they can put in our dataset. We show that our dataset captures
594 regional scale hourly, seasonal, and interannual variability in the meteorological variability well
595 across the CONUS. The model shows an excellent performance in simulating the regional and
596 temporal variability in temperature and relative humidity but a slightly poorer performance in
597 simulating winds and precipitation, which are well known shortcomings of the WRF model. The
598 model also shows a higher skill in reproducing variabilities in surface ozone (r = 0.77-0.91) than
599 $PM_{2.5}$ (0.49-0.79). The mean biases for CMAQ ozone and $PM_{2.5}$ are estimated to be 3.7-6.8 ppbv
600 and -0.9-5.6 $\mu g/m^3$, respectively, and the corresponding RMSE values are 7-9 ppbv and 3.0-8.3
601 $\mu g/m^3$, respectively.

602 The MDA8 ozone trend over CONUS is estimated to be -0.53 ± 0.46/-0.56 ± 0.45 ppb/year
603 (summertime) and -0.31 ± 0.43/-0.29 ± 0.39 ppb/year (annual), respectively, for AQS/CMAQ data
604 with ~70% of sites showing negative trends. At a 2-sigma level, the summertime MDA8 ozone
605 trends are -0.85 ± 0.36/-0.75 ± 0.35 ppb/year and annual MDA8 ozone trends are -0.52 ± 0.45/-
606 0.47 ± 0.42 ppb/year, respectively, for AQS/CMAQ data over CONUS. Annually, at 2-sigma level,
607 46% sites showed negative trends in both the data. Annual mean $PM_{2.5}$ trends are –0.24 ± 0.21/-
608 0.24 ± 0.24 $\mu g/m^3$/year, respectively in AQS/CMAQ data sets, and ~79% of the sites showed

Deleted:

negative trends. Annually, at 2-sigma level, 66% sites showed negative trends in both the data. During summertime, the negative trend percent is reduced to 71%, where an increase in positive trends are observed in the northwestern US.

An air quality dashboard has been developed, which provides a step-by-step path for users to explore information at the CONUS, state, and county levels. This dashboard allows the users to visualize air quality information in the form of maps, bar charts, and the NAAQS exceedance days. Finally, a Python-based Streamlit application is developed to allow the download of the air quality data in simplified text and graphic formats for the end user's choice of the region and time of interest.

8. Figures

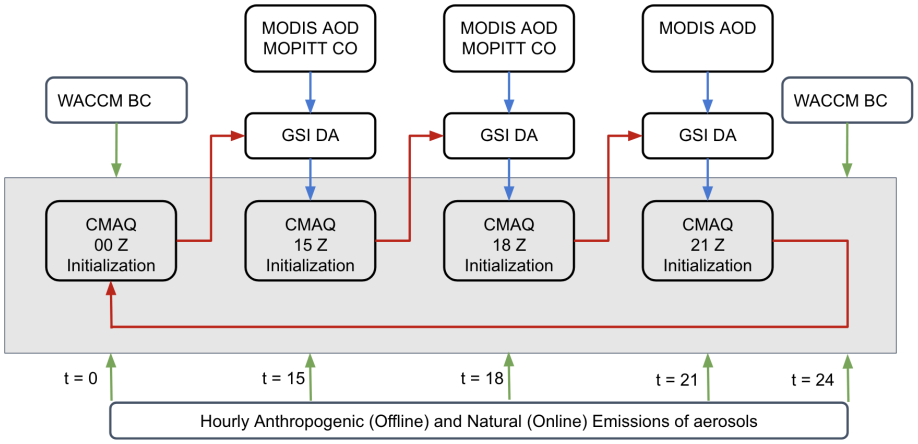

Figure 1: *Architecture of the daily GSI/CMAQ based chemical data assimilation workflow.*

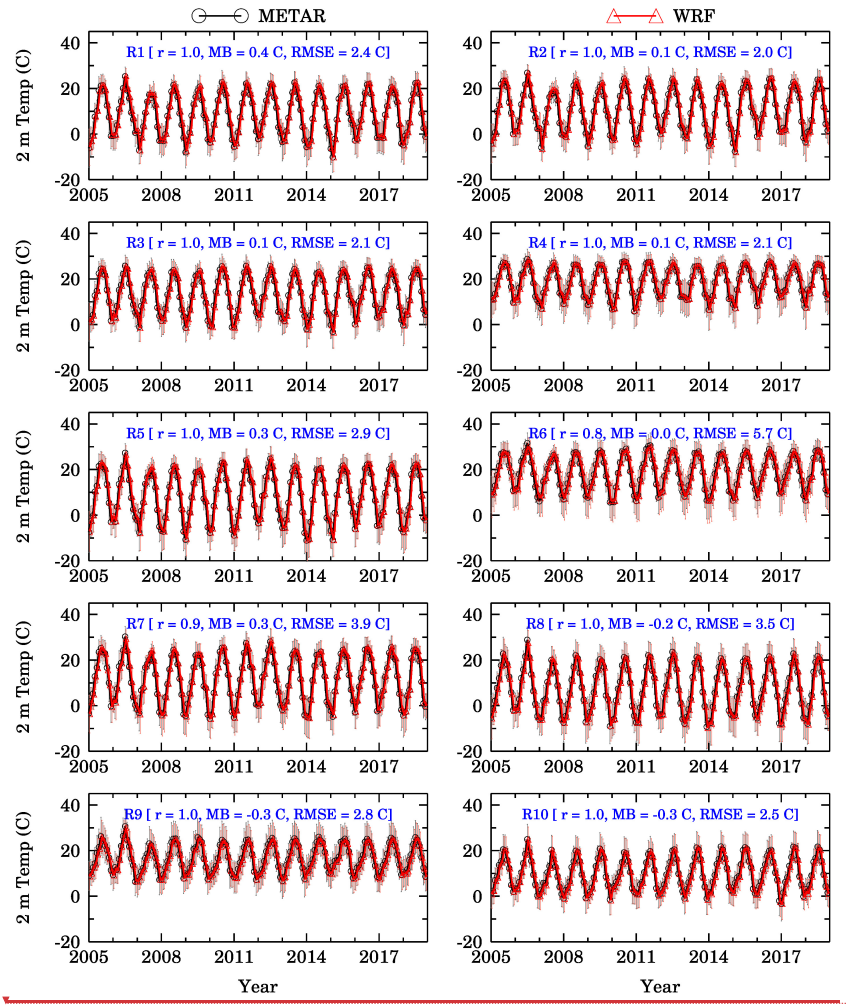

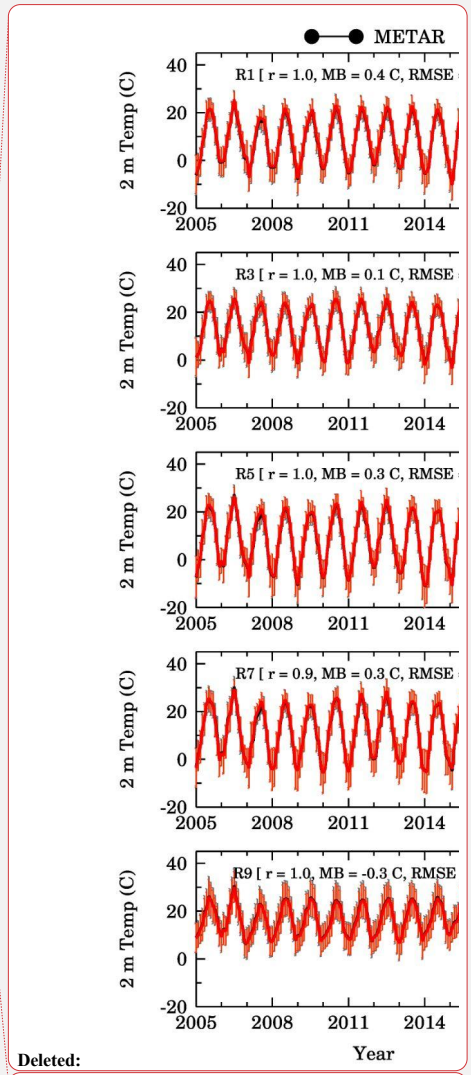

Figure 2: Time series of monthly averaged 2 m temperature over 10 EPA regions (R1-R10) from WRF-CMAQ setup (red) and METAR observations (black) during 2005-2018. Orange and Grey lines represent the standard deviation for WRF-CMAQ and METAR, respectively. The correlation coefficient (r), mean bias (MB), and the root mean square error (RMSE) for each region is also shown.

Deleted:

Formatted: Centered

Deleted: hourly

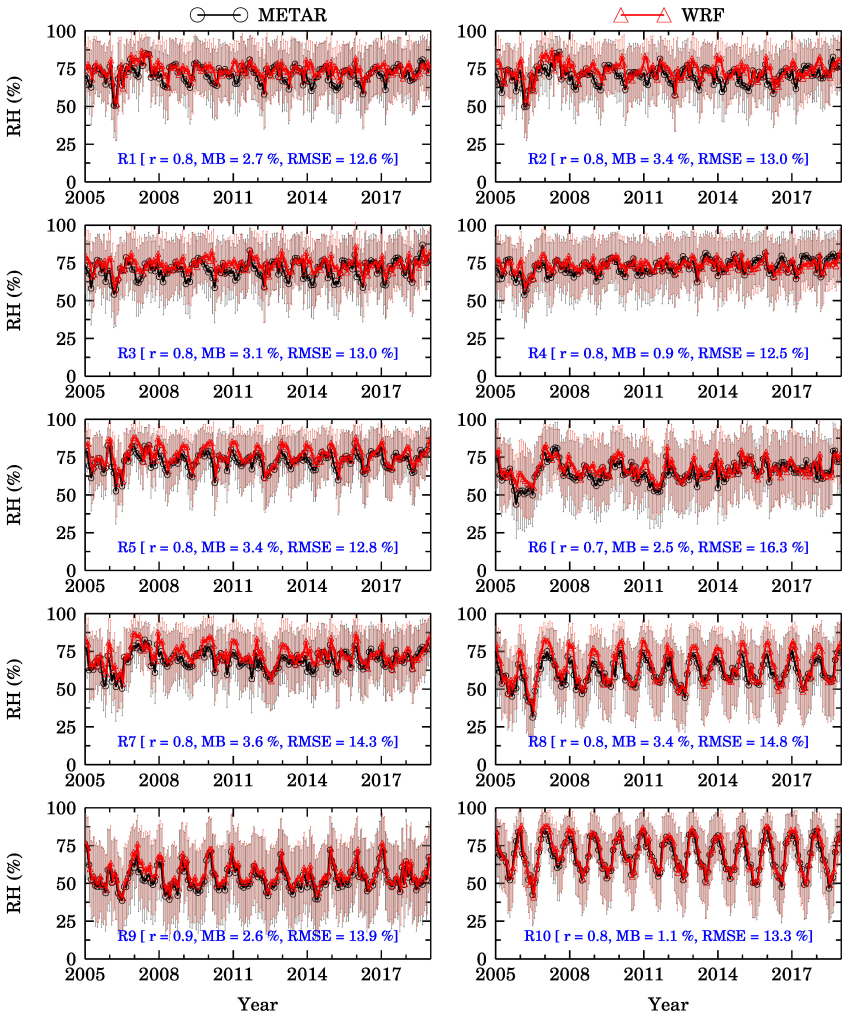

Figure 3: Same as Figure 2 but for 2 m relative humidity (RH).

Deleted:

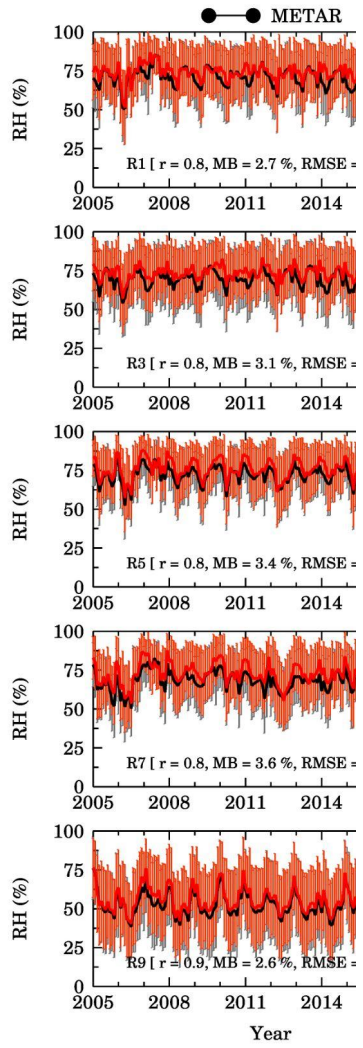

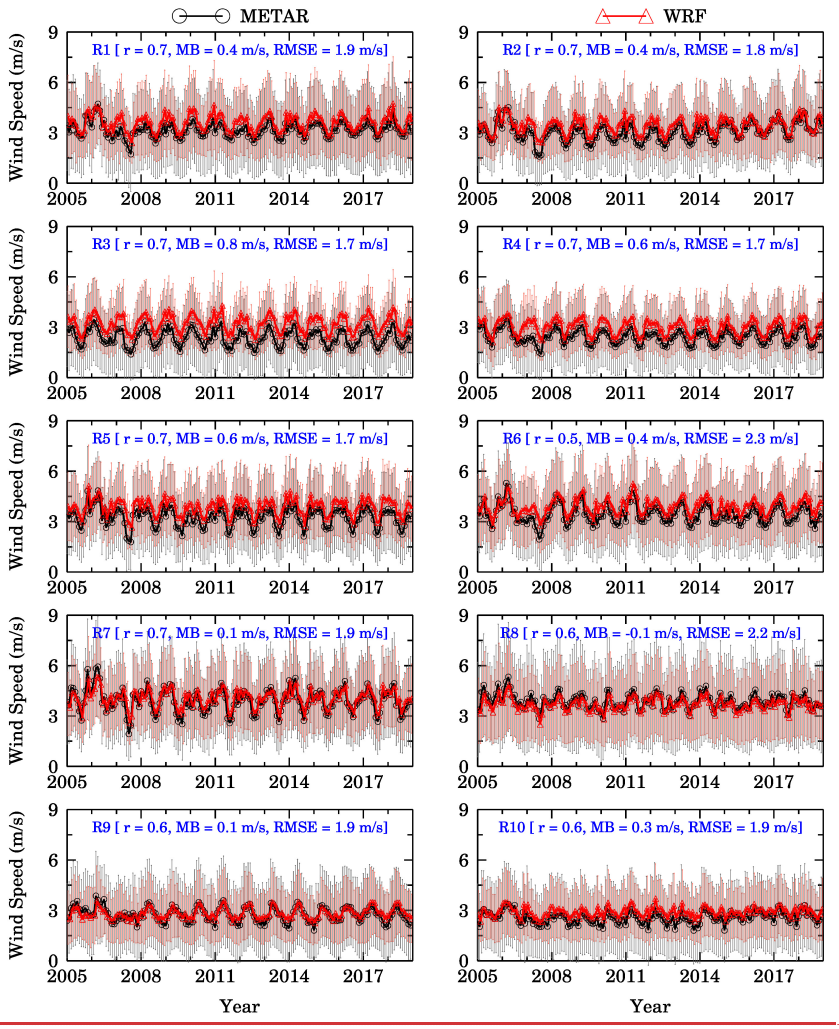

Deleted:

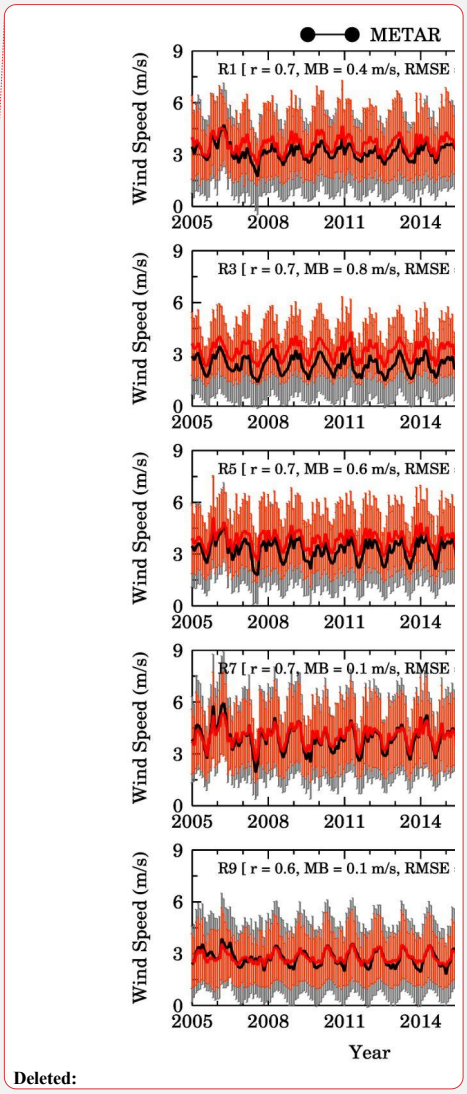

Figure 4: Same as Figure 2 but for 10 m wind speed.

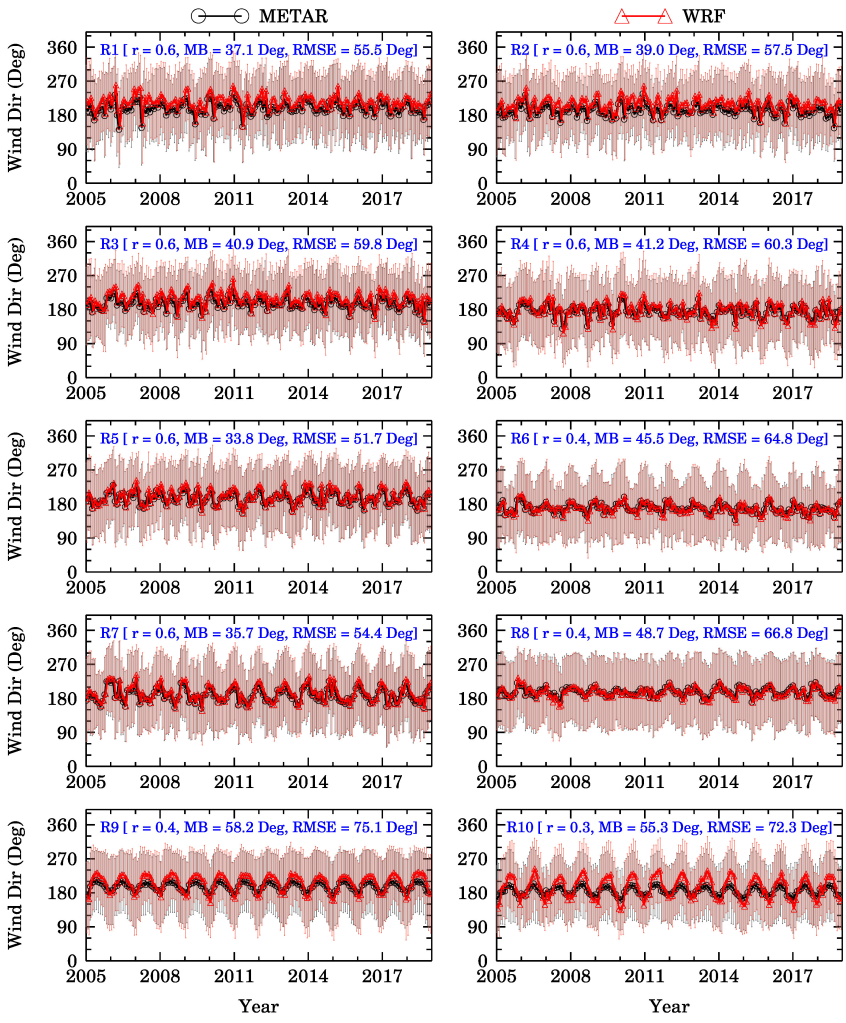

Figure 5: Same as Figure 2 but for 10 m wind direction.

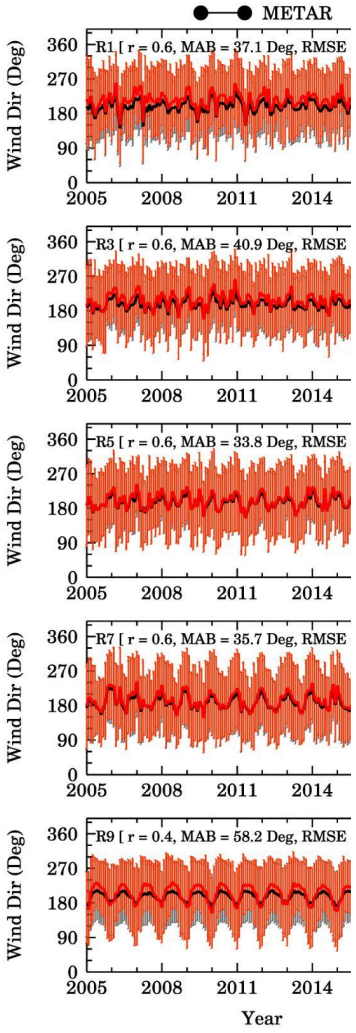

Deleted:

Deleted: Time series of hourly averaged 2 m temperature over 10 EPA regions (R1-R10) from WRF-CMAQ setup (red) and METAR observations (black) during 2005-2018. Orange and Grey lines represent standard deviation for WRF-CMAQ and METAR, respectively. The correlation coefficient (r), mean absolute bias (MAB), and the root mean square error (RMSE) for each region is also shown.

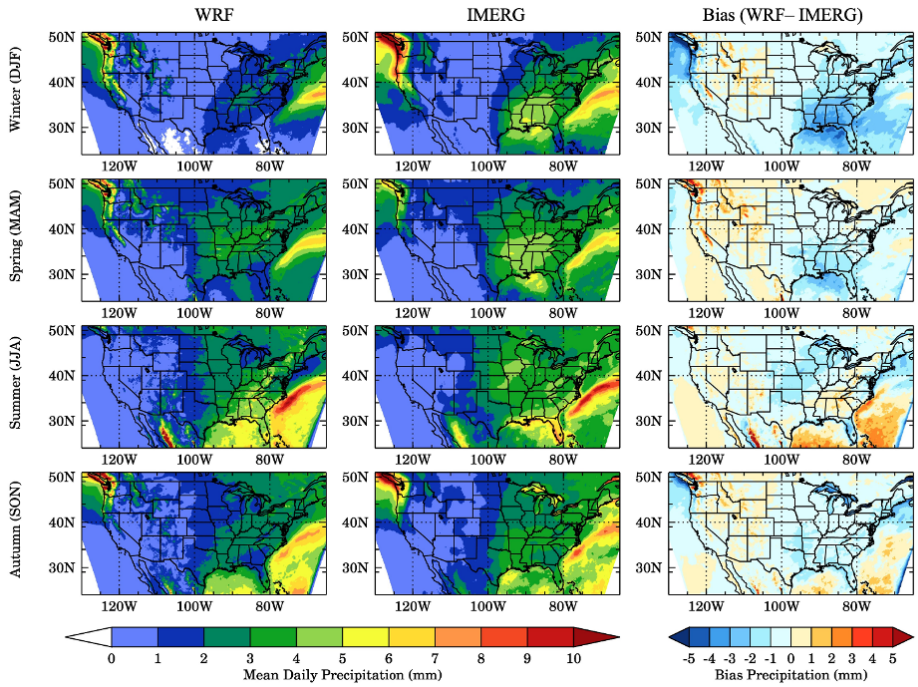

657

658 **Figure 6:** Spatial distribution of mean daily precipitation and bias during four seasons in 2005-
659 2018 (top to bottom, *viz.,* Winter, Spring, Summer and Autumn). Left, center and right panels
660 represent mean precipitation from WRF, IMERG and bias (WRF-IMERG) precipitation,
661 respectively.

662

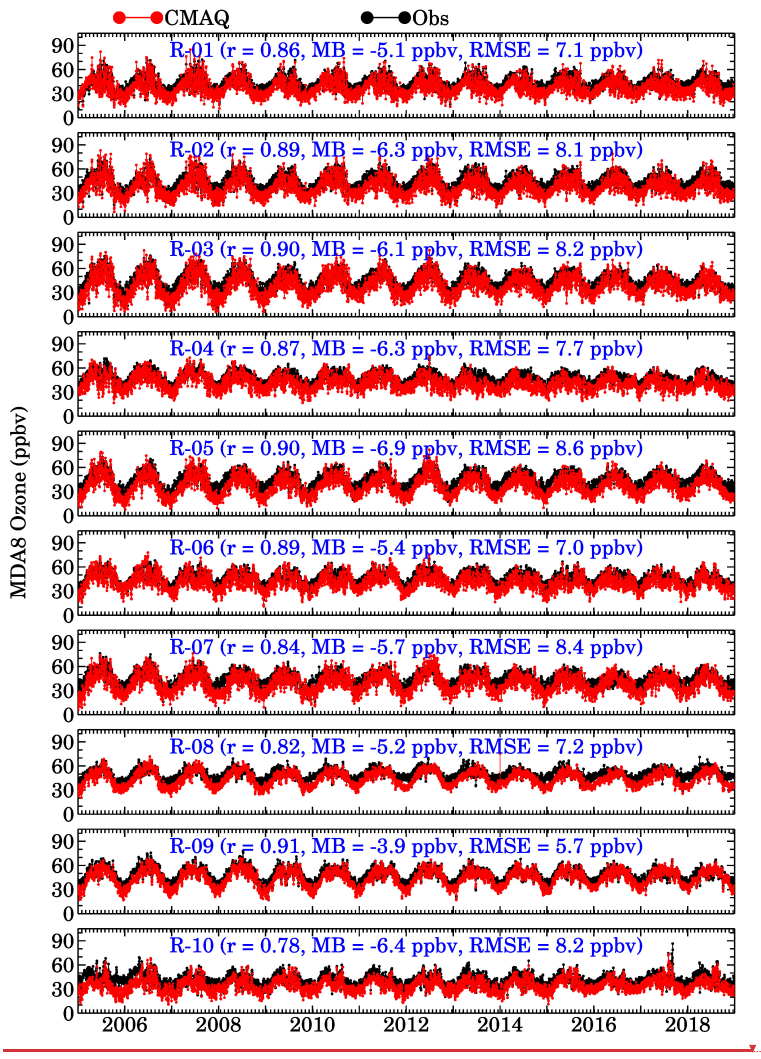

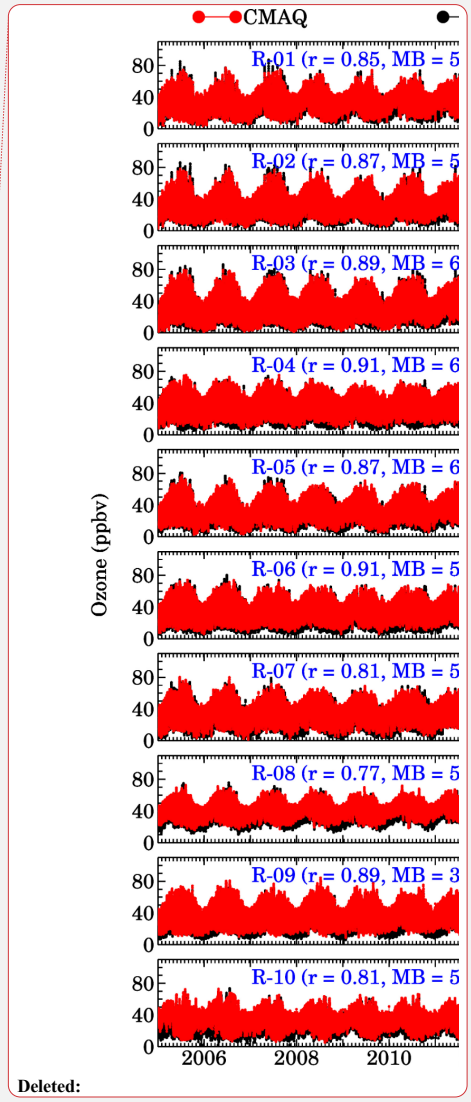

Deleted:

Figure 7: Time series of hourly averaged surface ozone over 10 EPA regions (R1-R10) from WRF-CMAQ setup (red) and EPA AQS observations (black) during 2005-2018. The correlation coefficient (r), mean bias (MB), and the root mean square error (RMSE) for each region is also shown.

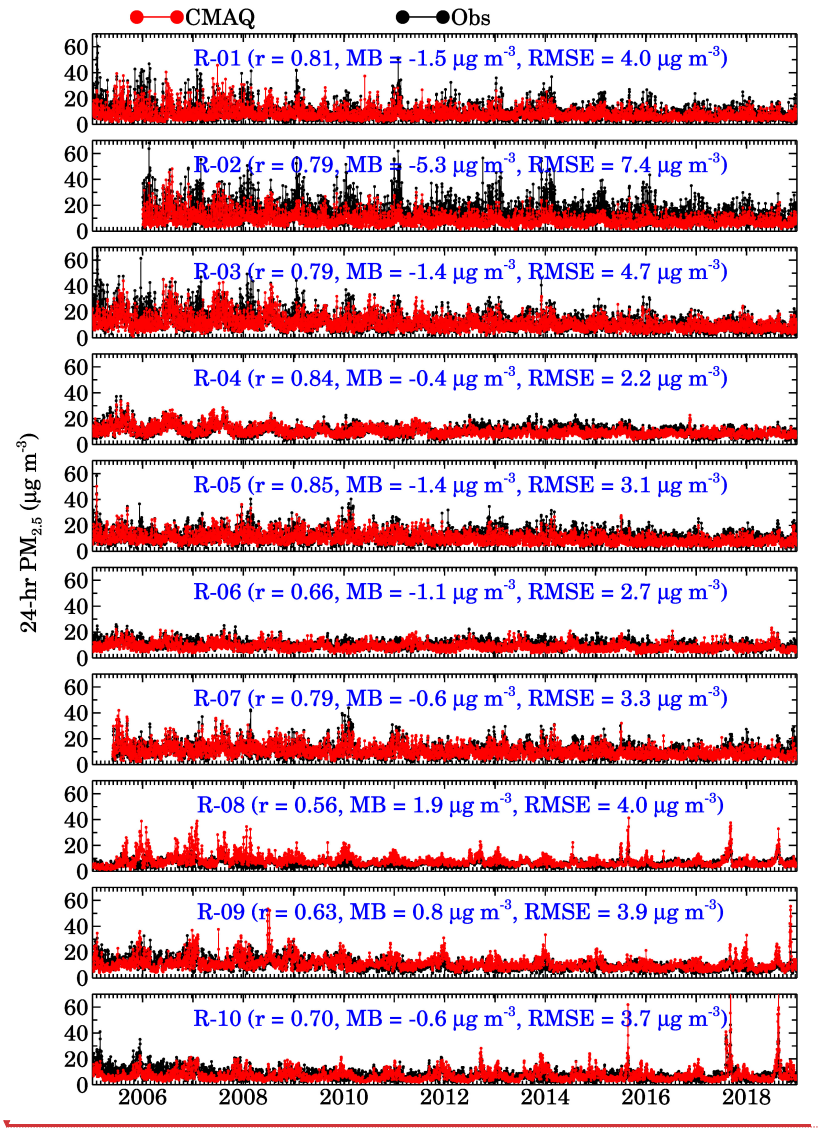

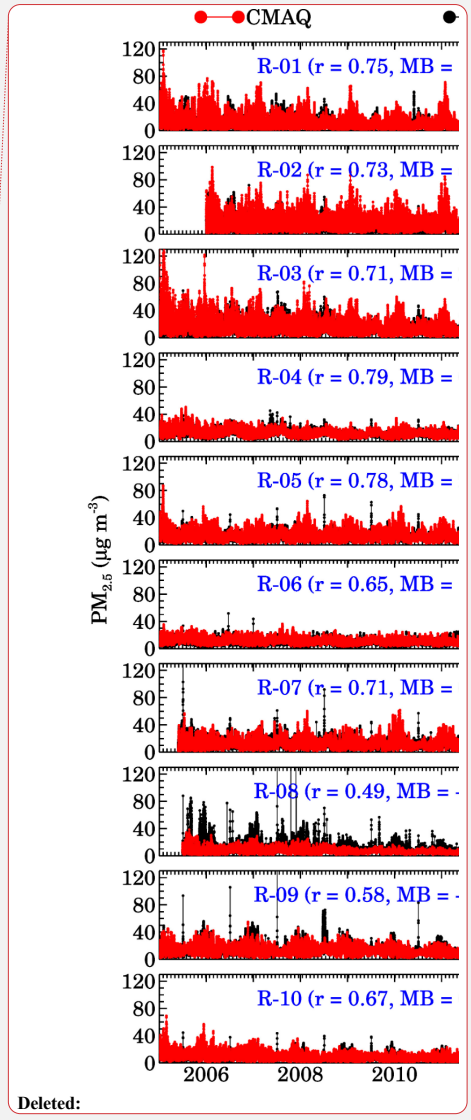

Deleted:

Figure 8: Same as Figure 7 but for daily averaged surface fine particulate matter ($PM_{2.5}$).

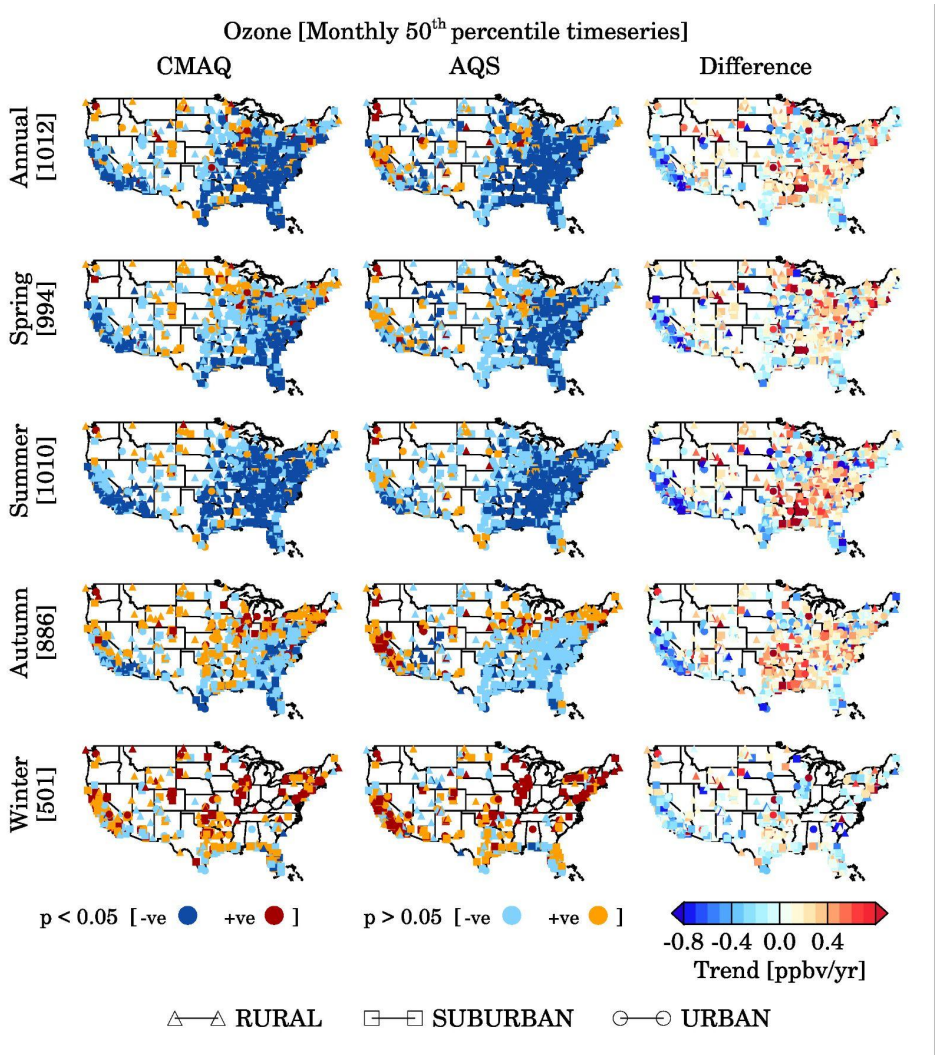

673

674 **Figure 9:** Spatial distribution of positive (blue colors), negative trends (red colors) in MDA8 ozone
675 at different statistically significant levels (p-values) using annual, seasonal monthly median time
676 series (top to bottom). Plots on the right show differences in trend values [CMAQ-AQS].

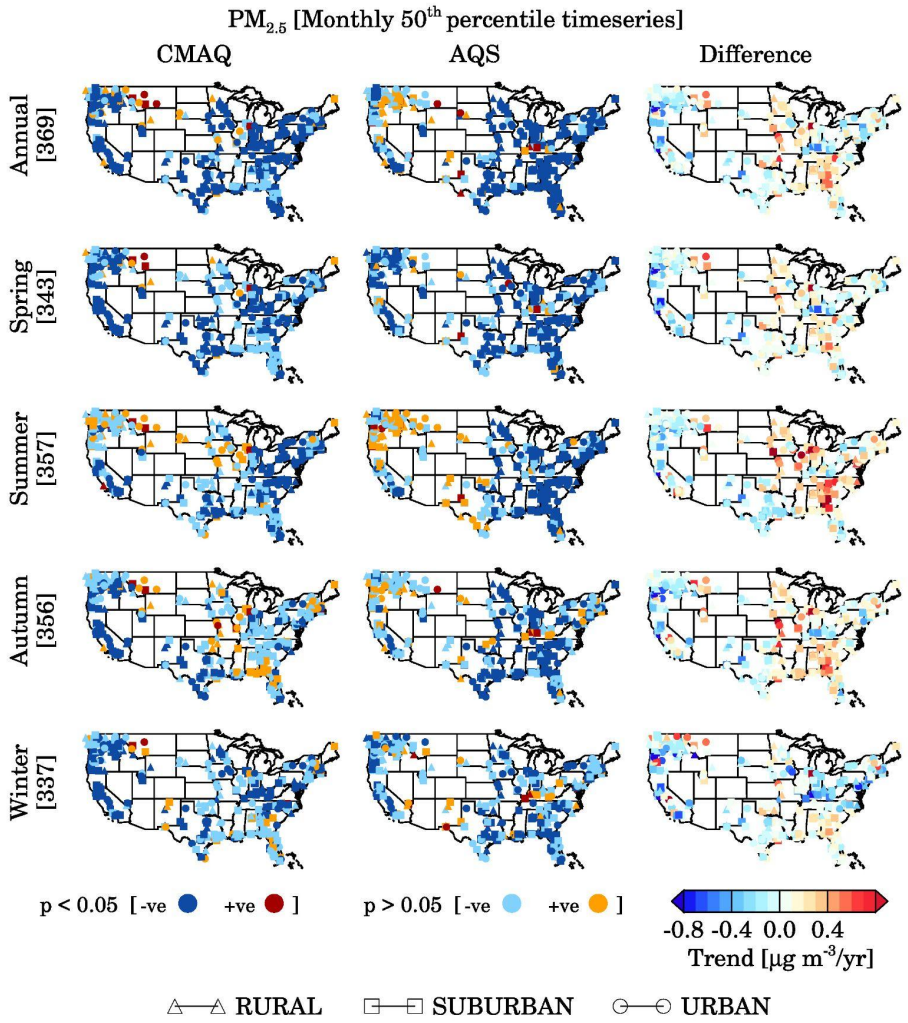

677

678 **Figure 10:** Spatial distribution of positive (blue colors), negative trends (red colors) in 24-hour
679 avg. $PM_{2.5}$ (right panel) at different statistically significant levels (p-values) using monthly median
680 time series (top to bottom). Plots on the right show differences in trend values [CMAQ-AQS].

681

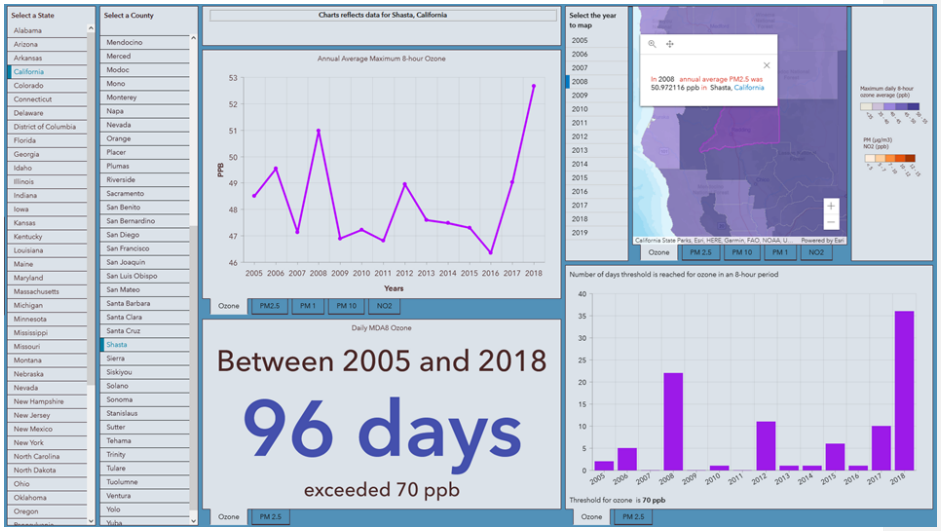

Figure 11: Dashboard reflecting Ozone concentrations for Shasta, CA.

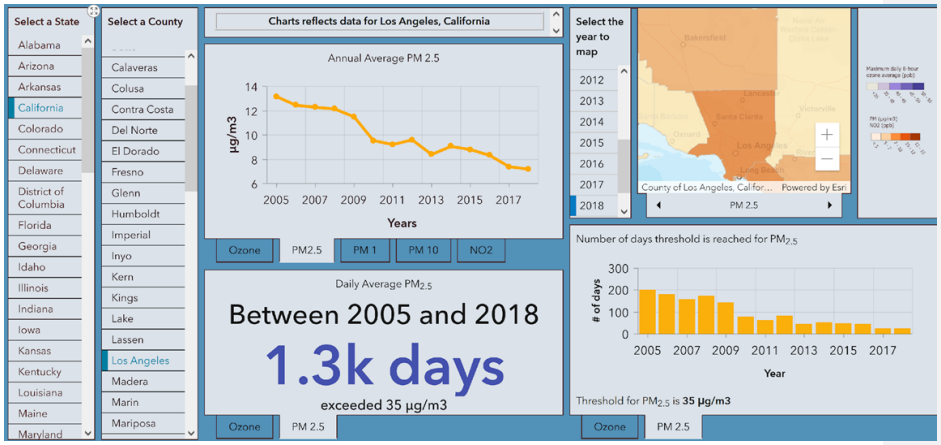

Figure 12: $PM_{2.5}$ concentrations for Los Angeles, CA.

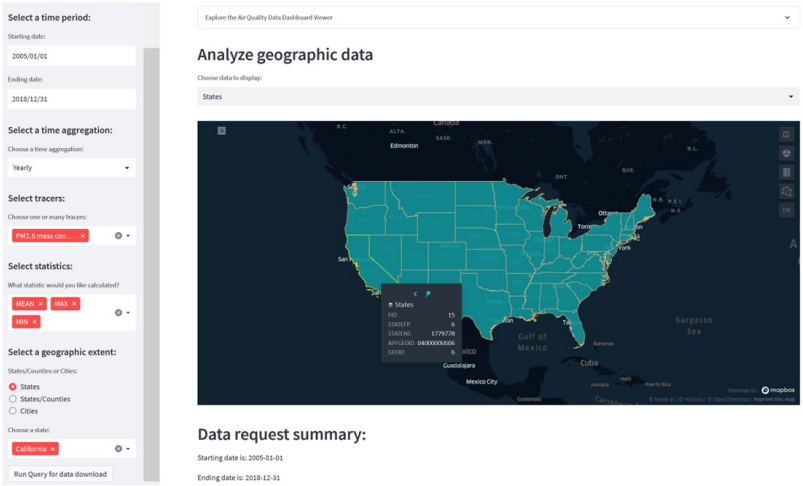

Figure 13: Streamlit Air Quality App to easily download and summarize data in a CSV format.

9. Appendices

A1: Forward and Adjoint operators for MOPITT CO assimilation

MOPITT retrieved profile consists of 10 levels, including a surface level followed by 100 hPa thick layers from 900 hPa to 100 hPa. The CMAQ vertical profile of CO cannot be compared with MOPITT CO directly and needs to be convolved with the MOPITT a priori profile and averaging kernel. Following (Barré et al., 2015; Gaubert et al., 2016), the CMAQ profile that can be compared directly to MOPITT can be written as:

$$CO_{ret}^{CMAQ} = 10^{(AK^{MOPITT} log_{10}(CO^{CMAQ}) + (I - AK^{MOPITT}) log_{10}(CO_{apr}^{MOPITT}))} \quad (1)$$

CO_{ret}^{CMAQ} is the CMAQ CO profile convolved with MOPITT a priori averaging kernel (AK^{MOPITT}) and a priori profile (CO_{apr}^{MOPITT}) that can be compared directly to the MOPITT retrieved CO profile. CO^{CMAQ} is the 10-layer CMAQ profile mapped to the MOPITT pressure grid. A log_{10} transformation is necessary because the averaging kernel matrix for retrievals is obtained with CO parameters in log_{10}(CO). Differentiation of equation (1) will yield the sensitivity of CO_{ret}^{CMAQ} with respect to CO^{CMAQ}, which represents the adjoint of the forward operator. For the purpose of derivation, let $CO_{ret}^{CMAQ} = y$; $CO^{CMAQ} = x$; $AK^{MOPITT} = A$; and $(I - AK^{MOPITT}) log_{10}(CO_{apr}^{MOPITT}) = C$ then equation (1) can be written as:

$$y = 10^{(Alog_{10}(x) + C)} \quad (2)$$

Applying the differentiation rule $\frac{d\,[a^u]}{dx} = ln(a) \cdot a^u \cdot \frac{du}{dx}$; we can differentiate equation (2) as:

$$\frac{dy}{dx} = ln(10) \cdot 10^{(Alog_{10}(x) + C)} \cdot \frac{d}{dx}(Alog_{10}(x) + C) \quad (3)$$

Since A and C do not depend on CMAQ simulations, they are constants and thus their differentiation is zero. Since $\frac{d}{dx}(log_{10}(x)) = \frac{1}{x\,ln(10)}$, equation (3) simplifies to

$$\frac{dy}{dx} = 10^{(A\log_{10}(x)+C)} \cdot A \cdot \frac{1}{x} = A \cdot \frac{y}{x} \quad (4)$$

Substituting the values of $y, x, A, and\ C$ in equation (4), the changes in CO vertical profile in the MOPITT space can be related to changes in CO vertical profile in CMAQ as follows:

$$dCO_{ret}^{CMAQ} = AK^{MOPITT} \cdot \frac{CO_{ret}^{CMAQ}}{CO^{CMAQ}} dCO^{CMAQ} \quad (5)$$

By writing equation (5) in matrix form and then transposing the forward operator matrix, we can write the adjoint of the forward operator as a recursive matrix equation:

$$dCO^{CMAQ} = dCO^{CMAQ} + AK^{MOPITT} \cdot \frac{CO_{ret}^{CMAQ}}{CO^{CMAQ}} dCO_{ret}^{CMAQ} \quad (6)$$

A2: Additional Figures

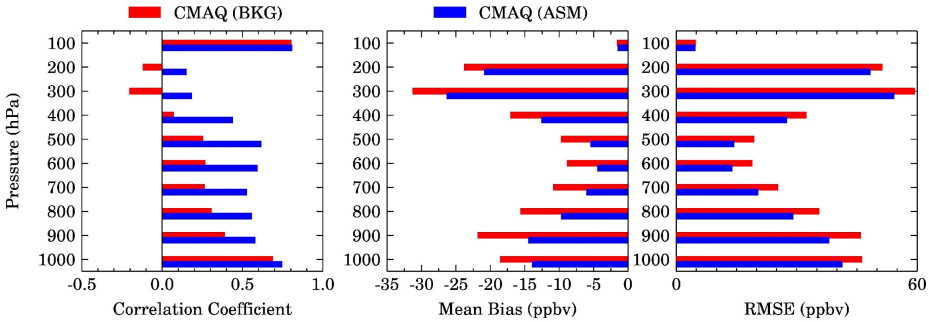

Figure A2.1: Correlation coefficient, Mean bias, and Root Mean Squared Error (RMSE) between CMAQ and MOPITT CO profiles at ten MOPITT retrievals pressure levels for the CMAQ experiments with (ASM) and without (BKG) assimilation of the MOPITT CO profiles during July 2018. These statistics are based on 118552 data points at each level.

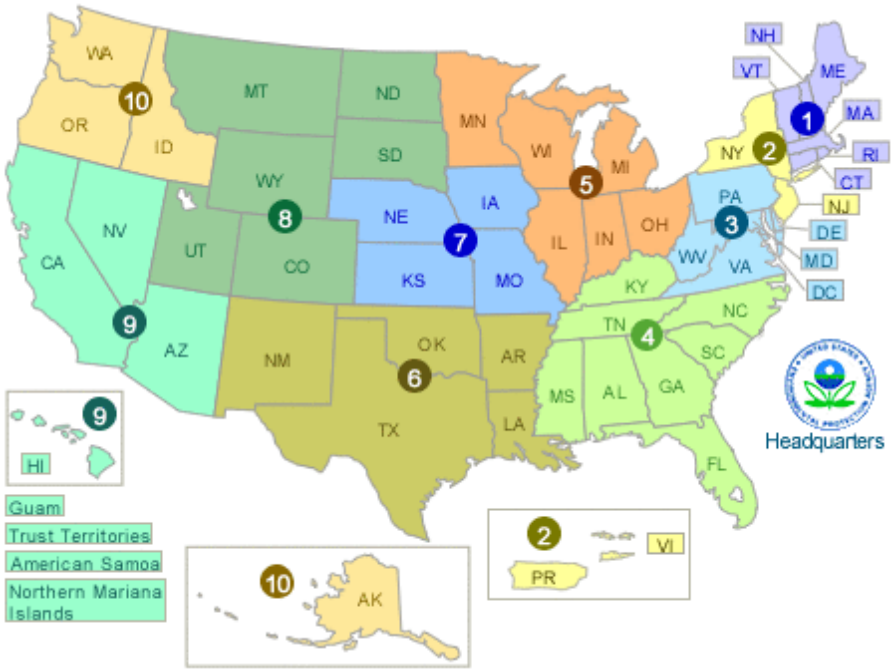

Figure A2.2: Map showing the EPA regions over which model evaluation has been performed. The map is reproduced from https://www.epa.gov/aboutepa/visiting-regional-office. Our evaluation does not include Puerto Rico in Region 2, Hawaiian Islands in Region 9, and Alaska in Region 10.

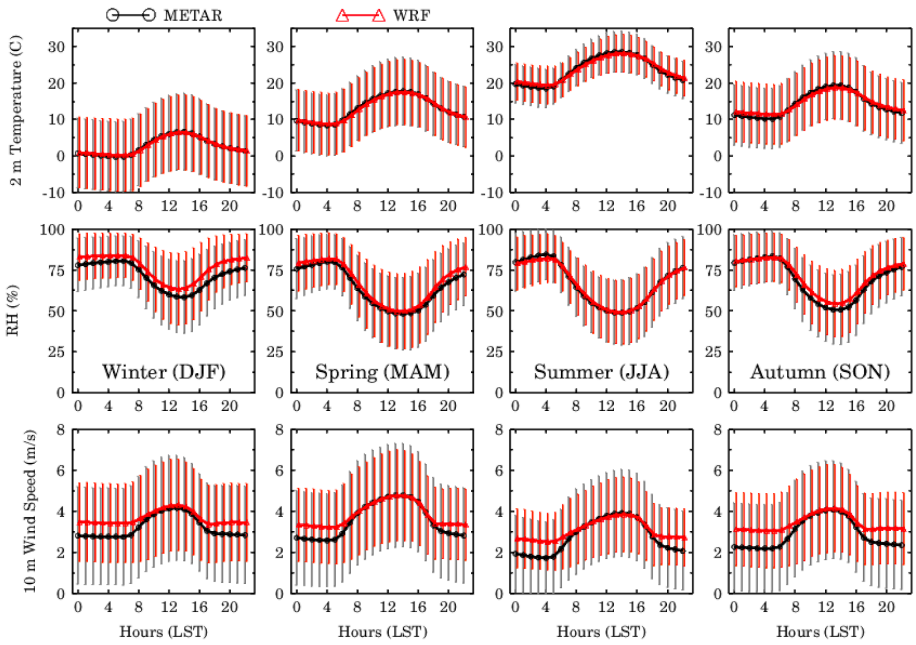

Figure A2.3: Seasonal mean diurnal variations in 2 m Temperature (Top panel), relative humidity (middle panel) and 10 m wind speed (bottom panel) from METAR observations and WRF model.

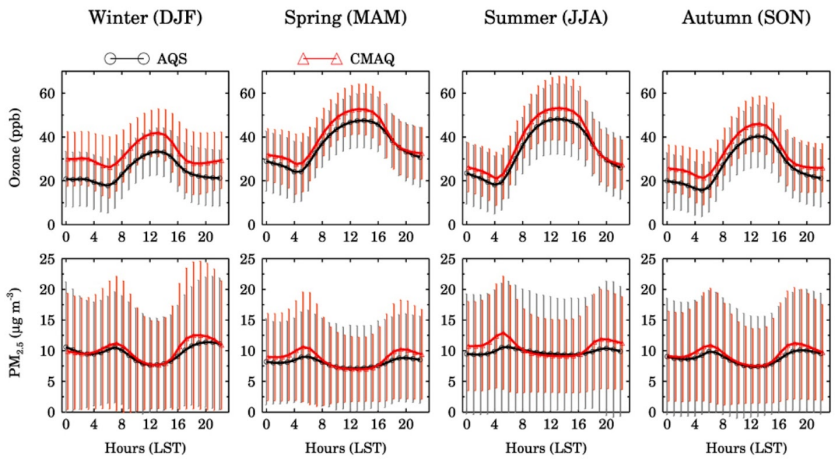

Figure A2.4: Average diurnal profile of ozone (top panel) and $PM_{2.5}$ (bottom panel) over all AQS sites in CONUS.

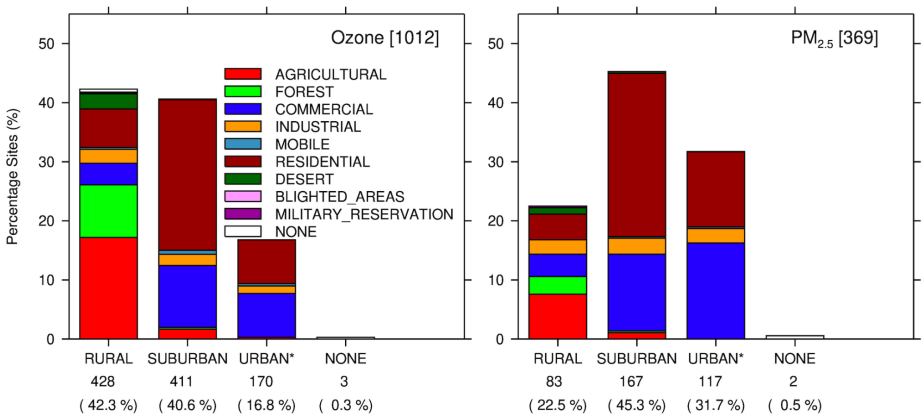

Figure A2.5: The stacked histogram shows the number of sites in each location setting (different bars) and land use type (different colors) for MDA8 ozone (left) and 24-hr avg. $PM_{2.5}$ (right).

Deleted: 2

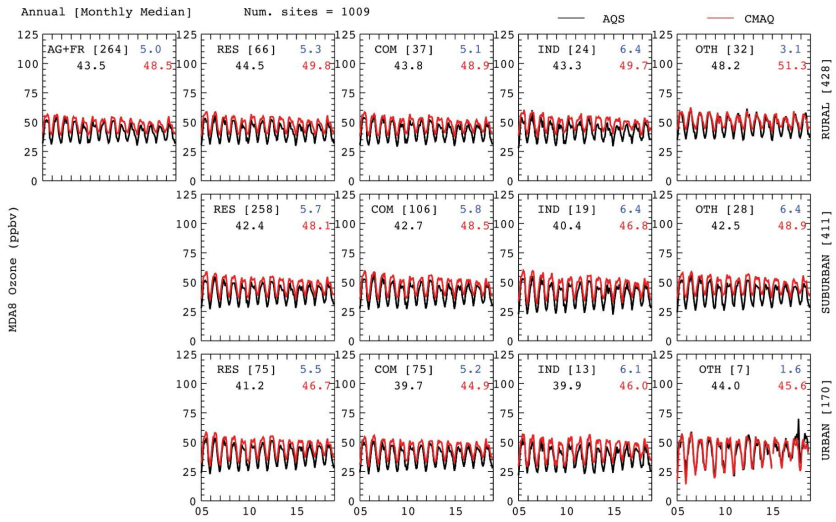

Figure A2.6: The Annual mean (derived from monthly median values) time series of MDA8 Ozone using AQS data (black) and CMAQ (red) over different location type (top to bottom) and land-use type (left to right) during 2005-2018. The number of sites for each scenario are presented in brackets. The blue color represents the mean bias.

Deleted: 3

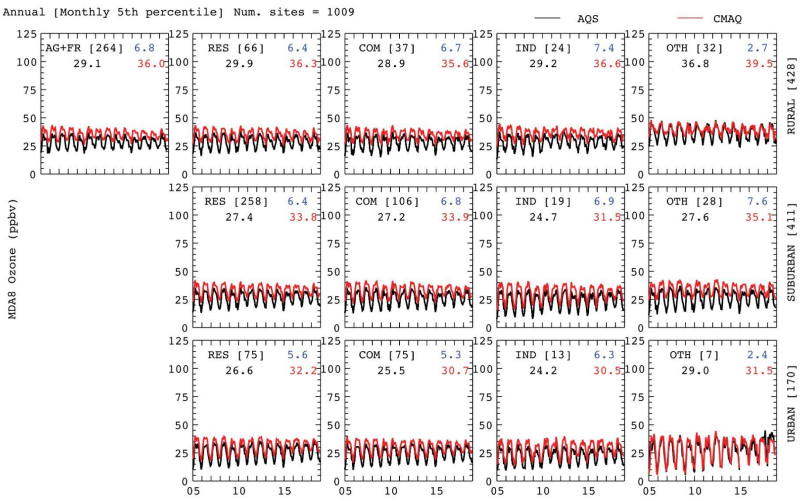

768

769 **Figure A2.7:** Same as Figure A2.6 but time series is derived from monthly 5th percentile values

770

771

Deleted: 4

Deleted: 3

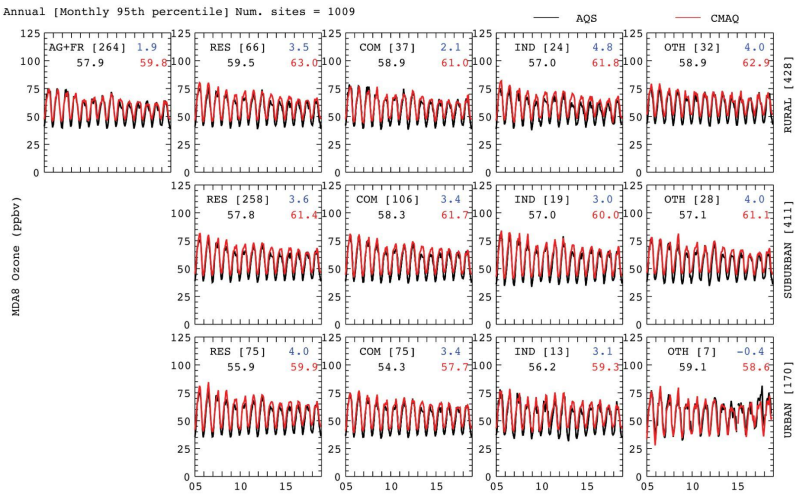

774

775 **Figure A2.8:** Same as Figure A2.6 but time series is derived from monthly 95th percentile values.

776

777

Deleted: 5

Deleted: 3

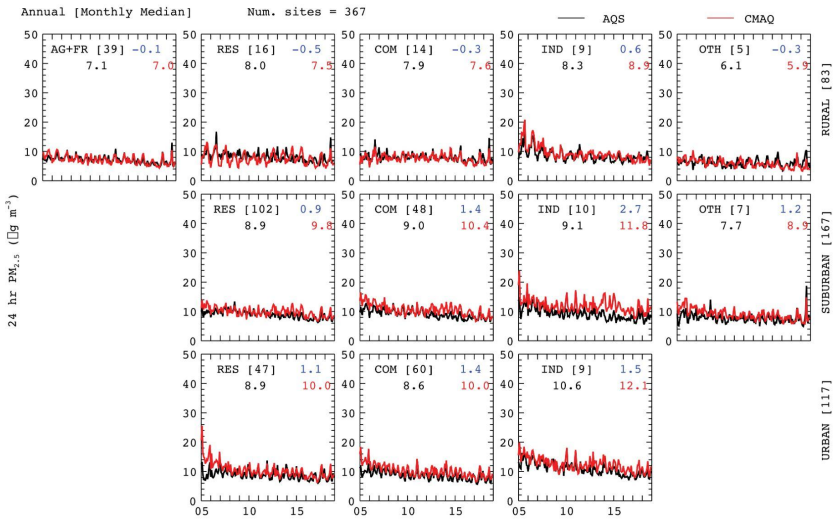

780

781 **Figure A2.9:** The Annual mean (derived from monthly values) time series of 24-hour avg. $PM_{2.5}$

782 using AQS data (black) and CMAQ (red) over different location types (top to bottom) and land-

783 use type (left to right) during 2005-18. The number of sites for each scenario are presented in

784 brackets. The blue color represents the mean bias.

785

786

Deleted: 6

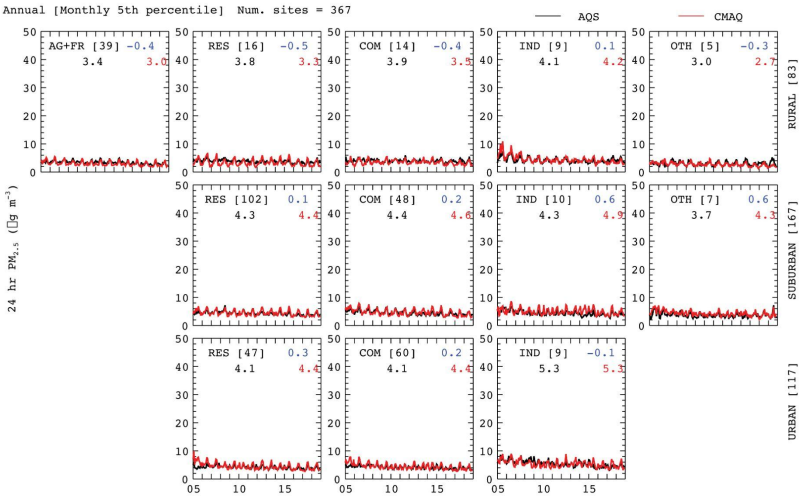

788

789 **Figure A2.10:** Same as Figure A2.9 but time series is derived from monthly 5th percentile values.

790

791

Deleted: 7

Deleted: 6

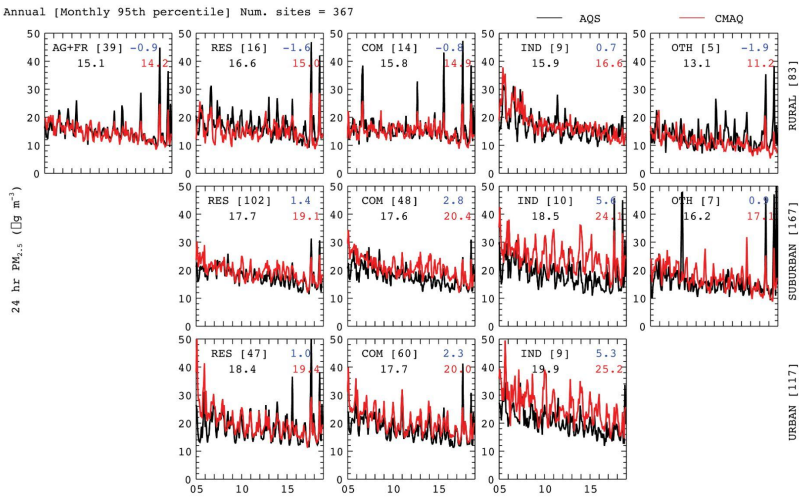

Figure A2.11: Same as Figure A2.9 but time series is derived from monthly 95th percentile values.

Deleted: 8

Deleted: 6

A3: Additional Tables

Table A3.1: Key physics and chemical schemes used in the WRF-CMAQ configuration.

Physics	**Setup-1 (standard simulation used for assimilation)**	**Setup-2 (sensitivity simulation used to generate background error)**
Long-wave radiation	RRTMG	RRTM Longwave
Short-wave radiation	RRTMG	Goddard Shortwave
Microphysics	Morrison double-moment	Thomson
Cumulus	Kain–Fritsch version 2	Grell 3-D ensemble
Land surface model	Pleim–Xiu LSM	Unified Noah LSM
Surface Layer	Pleim–Xiu surface layer	MYNN
PBL	ACM2	MYNN level 2.5
Gas-phase chemistry	CB06	CB06
Aerosol chemistry	AERO7	AERO7
Anthropogenic and fire emissions	EPA NEI	EPA NEI perturbed by factors* derived from uncertainty analysis of multiple emission datasets
Biogenic emission	Online CMAQ BEIS	Offline MEGAN

Deleted: ¶
Page Break

Table A3.2: Annual anthropogenic emissions for nine species over CONUS during 2005-2018.

Emissions (Tg/yr)	HTAP v2 [2010]	EDGAR v4.3.2 [2010]	MACCity [2005-16]	CAMSv4.2 [2005-16]	NEI+ [2014]	Min-Max Ratio
CO	56.20	56.77	46.02 ± 6.39	56.49 ± 6.46	45.69	**1.24**
NH_3	4.42	5.14	4.44 ± 0.14	5.12 ± 0.07	3.25	**1.58**
NO_x	11.07	10.93	10.40 ± 1.00	10.46 ± 0.96	12.03	**1.16**
SO_2	13.10	12.52	10.87 ± 2.44	11.48 ± 1.90	4.46	**2.94**
CH_2O	0.12	0.20	0.17 ± 0.02	0.26 ± 0.02	0.16	**2.17**
NMVOC	15.61	14.57	6.58 ± 0.82	14.92 ± 0.74	12.28	**2.37**
OC	0.61	0.36	0.48 ± 0.08	0.36 ± 0.01	0.79**	**2.19**
BC	0.34	0.20	0.28 ± 0.06	0.21 ± 0.02	0.26**	**1.70**
$PM_{2.5}$	2.02	N/A	N/A	N/A	3.67	**1.82**

[+] Except NEI, all other emissions are simply summed over {20-50 N} & {60-130 W} region

** CONUS $PM_{2.5}$ emissions are 5.15 Tg/yr which has 8% BC (or EC) and 28% OC

https://www.epa.gov/sites/production/files/2019-08/documents/210pm_rao_508_2.pdf

821 **Table A3.3:** Annual biomass burning emissions for nine species over the CONUS during 2005-
822 2018.

Emissions (Tg/yr)	Top-Down emissions		Bottom-up emissions			Min-Max Ratio
	QFED	GFASv1.3	FINNv1.5	GFEDv4.1	NEI	
CO	12.90 ± 2.59	8.99 ± 2.40	10.93 ± 2.21	5.41 ± 1.12	16.95	**3.13**
NH_3	0.56 ± 0.11	0.12 ± 0.03	0.18 ± 0.04	0.07 ± 0.02	0.27	**8.00**
NO_x	0.56 ± 0.11	0.20 ± 0.06	0.47 ± 0.10	0.18 ± 0.04	0.25	**3.11**
SO_2	0.32 ± 0.07	0.07 ± 0.02	0.09 ± 0.02	0.04 ± 0.01	0.13	**8.00**
CH_2O	0.16 ± 0.03	0.15 ± 0.04	0.15 ± 0.03	0.10 ± 0.02	0.22	**2.20**
tVOC	0.53 ± 0.11	1.05 ± 0.28	1.86 ± 0.40	1.06 ± 0.22	3.92	**7.40**
OC	2.99 ± 0.63	0.60 ± 0.17	0.66 ± 0.13	0.34 ± 0.09	0.45	**8.79**
BC	0.24± 0.05	0.05 ± 0.02	0.06 ± 0.01	0.03 ± 0.01	0.15	**8.00**
$PM_{2.5}$	4.37 ± 0.92	0.90 ± 0.24	N/A	0.61 ± 0.14	1.48	**7.16**

823

10. Author contribution

RK, PB, CH, GGP, SA, HW, and OG conceptualized the study. All the authors contributed to the design of the study. RK, CH, and PB performed all the model simulations including the data assimilation system developments and experiments. PB, CH, RK, and SA contributed to the model evaluation and trend analysis. RK, FL, JB, OG, KS, MC, and SS contributed to the design of the air quality dashboard and Streamlit application. RK prepared the first draft of the paper. All authors contributed to the editing of the manuscript.

11. Competing interests

The authors do not have any competing interests. The funding agency had no role in the design of the study, in the collection, analyses, interpretation of data, in the writing of the manuscript, or in the decision to publish the results.

12. Financial support

This work is supported by the NASA Atmospheric Composition Modeling and Analysis (ACMAP) Grant # 80NSSC19K0982.

13. Acknowledgement

We would like to acknowledge high-performance computing support from Cheyenne (doi: 10.5065/D6RX99HX (accessed on 08 June 2023)), provided by NCAR's Computational and Information Systems Laboratory, sponsored by the National Science Foundation. This material is based upon work supported by the NSF National Center for Atmospheric Research, which is a

major facility sponsored by the U.S. National Science Foundation under Cooperative Agreement No. 1852977.

Deleted: The National Center for Atmospheric Research is sponsored by the National Science Foundation under Cooperative Agreement 1852977

Deleted: ¶
¶

14. References

Appel, K. W., Bash, J. O., Fahey, K. M., Foley, K. M., Gilliam, R. C., Hogrefe, C., Hutzell, W. T., Kang, D., Mathur, R., Murphy, B. N., Napelenok, S. L., Nolte, C. G., Pleim, J. E., Pouliot, G. A., Pye, H. O. T., Ran, L., Roselle, S. J., Sarwar, G., Schwede, D. B., Sidi, F. I., Spero, T. L., and Wong, D. C.: The Community Multiscale Air Quality (CMAQ) model versions 5.3 and 5.3.1: system updates and evaluation, Geoscientific Model Development, 14, 2867–2897, https://doi.org/10.5194/gmd-14-2867-2021, 2021.

Appel, K. W., Napelenok, S. L., Foley, K. M., Pye, H. O. T., Hogrefe, C., Luecken, D. J., Bash, J. O., Roselle, S. J., Pleim, J. E., Foroutan, H., Hutzell, W. T., Pouliot, G. A., Sarwar, G., Fahey, K. M., Gantt, B., Gilliam, R. C., Heath, N. K., Kang, D., Mathur, R., Schwede, D. B., Spero, T. L., Wong, D. C., and Young, J. O.: Description and evaluation of the Community Multiscale Air Quality (CMAQ) modeling system version 5.1, Geoscientific Model Development, 10, 1703–1732, https://doi.org/10.5194/gmd-10-1703-2017, 2017.

Appel, K. W., Pouliot, G. A., Simon, H., Sarwar, G., Pye, H. O. T., Napelenok, S. L., Akhtar, F., and Roselle, S. J.: Evaluation of dust and trace metal estimates from the Community Multiscale Air Quality (CMAQ) model version 5.0, Geoscientific Model Development, 6, 883–899, https://doi.org/10.5194/gmd-6-883-2013, 2013.

Appel, K. W., Roselle, S. J., Gilliam, R. C., and Pleim, J. E.: Sensitivity of the Community Multiscale Air Quality (CMAQ) model v4.7 results for the eastern United States to MM5 and WRF meteorological drivers, Geoscientific Model Development, 3, 169–188, https://doi.org/10.5194/gmd-3-169-2010, 2010.

Atmospheric Environment, Volume 300, 2023, 119693, ISSN 1352-2310, https://doi.org/10.1016/j.atmosenv.2023.119693.

Barré, J., Gaubert, B., Arellano, A. F. J., Worden, H. M., Edwards, D. P., Deeter, M. N., Anderson, J. L., Raeder, K., Collins, N., Tilmes, S., Francis, G., Clerbaux, C., Emmons, L. K., Pfister, G. G., Coheur, P.-F., and Hurtmans, D.: Assessing the impacts of assimilating IASI and MOPITT CO retrievals using CESM-CAM-chem and DART, Journal of Geophysical Research: Atmospheres, 120, 10,501-10,529, https://doi.org/10.1002/2015JD023467, 2015.

Bloomer, B. J., Vinnikov, K. Y., and Dickerson, R. R.: Changes in seasonal and diurnal cycles of ozone and temperature in the eastern U.S., Atmospheric Environment, 44, 2543–2551, https://doi.org/10.1016/j.atmosenv.2010.04.031, 2010.

Burke M., Childs M. L., de la Cuesta B., Qiu M., Li J., Gould C. F., Heft-Neal S., Wara M.: The contribution of wildfire to PM2.5 trends in the USA. Nature 622, 761–766. https://doi.org/10.1038/s41586-023-06522-6, 2023.

Butler, T. J., Vermeylen, F. M., Rury, M., Likens, G. E., Lee, B., Bowker, G. E., and McCluney, L.: Response of ozone and nitrate to stationary source NOx emission reductions in the eastern USA, Atmospheric Environment, 45, 1084–1094, https://doi.org/10.1016/j.atmosenv.2010.11.040, 2011.

Chang, K.-L., Petropavlovskikh, I., Cooper, O. R., Schultz, M. G., and Wang, T.: Regional trend analysis of surface ozone observations from monitoring networks in eastern North America, Europe and East Asia, Elementa: Science of the Anthropocene, 5, 50, https://doi.org/10.1525/elementa.243, 2017.

Cooper, O. R., Gao, R.-S., Tarasick, D., Leblanc, T., and Sweeney, C.: Long-term ozone trends

at rural ozone monitoring sites across the United States, 1990–2010, Journal of Geophysical Research: Atmospheres, 117, https://doi.org/10.1029/2012JD018261, 2012.

Deeter, M. N., Edwards, D. P., Francis, G. L., Gille, J. C., Mao, D., Martínez-Alonso, S., Worden, H. M., Ziskin, D., and Andreae, M. O.: Radiance-based retrieval bias mitigation for the MOPITT instrument: the version 8 product, Atmospheric Measurement Techniques, 12, 4561–4580, https://doi.org/10.5194/amt-12-4561-2019, 2019.

Dennison, P. E., Brewer, S. C., Arnold, J. D., and Moritz, M. A.: Large wildfire trends in the western United States, 1984–2011, Geophysical Research Letters, 41, 2928–2933, https://doi.org/10.1002/2014GL059576, 2014.

Di, Q., Wang, Y., Zanobetti, A., Wang, Y., Koutrakis, P., Choirat, C., Dominici, F., and Schwartz, J. D.: Air Pollution and Mortality in the Medicare Population, New England Journal of Medicine, 376, 2513–2522, https://doi.org/10.1056/NEJMoa1702747, 2017.

Fahey, K. M., Carlton, A. G., Pye, H. O. T., Baek, J., Hutzell, W. T., Stanier, C. O., Baker, K. R., Appel, K. W., Jaoui, M., and Offenberg, J. H.: A framework for expanding aqueous chemistry in the Community Multiscale Air Quality (CMAQ) model version 5.1, Geoscientific Model Development, 10, 1587–1605, https://doi.org/10.5194/gmd-10-1587-2017, 2017.

Fiore, A. M., Jacob, D. J., Bey, I., Yantosca, R. M., Field, B. D., Fusco, A. C., and Wilkinson, J. G.: Background ozone over the United States in summer: Origin, trend, and contribution to pollution episodes, Journal of Geophysical Research: Atmospheres, 107, ACH 11-1-ACH 11-25, https://doi.org/10.1029/2001JD000982, 2002.

Fleming, Z. L., Doherty, R. M., Schneidemesser, E. von, Malley, C. S., Cooper, O. R., Pinto, J. P., Colette, A., Xu, X., Simpson, D., Schultz, M. G., Lefohn, A. S., Hamad, S., Moolla,

R., Solberg, S., and Feng, Z.: Tropospheric Ozone Assessment Report: Present-day ozone distribution and trends relevant to human health, Elem Sci Anth, 6, 12, https://doi.org/10.1525/elementa.273, 2018.

Gan, C.-M., Pleim, J., Mathur, R., Hogrefe, C., Long, C. N., Xing, J., Wong, D., Gilliam, R., and Wei, C.: Assessment of long-term WRF–CMAQ simulations for understanding direct aerosol effects on radiation "brightening" in the United States, Atmospheric Chemistry and Physics, 15, 12193–12209, https://doi.org/10.5194/acp-15-12193-2015, 2015.

Gaubert, B., Arellano, A. F., Barré, J., Worden, H. M., Emmons, L. K., Tilmes, S., Buchholz, R. R., Vitt, F., Raeder, K., Collins, N., Anderson, J. L., Wiedinmyer, C., Alonso, S. M., Edwards, D. P., Andreae, M. O., Hannigan, J. W., Petri, C., Strong, K., and Jones, N.: Toward a chemical reanalysis in a coupled chemistry-climate model: An evaluation of MOPITT CO assimilation and its impact on tropospheric composition, Journal of Geophysical Research: Atmospheres, 121, 7310–7343, https://doi.org/10.1002/2016JD024863, 2016.

Gaubert, B., Worden, H. M., Arellano, A. F. J., Emmons, L. K., Tilmes, S., Barré, J., Alonso, S. M., Vitt, F., Anderson, J. L., Alkemade, F., Houweling, S., and Edwards, D. P.: Chemical Feedback From Decreasing Carbon Monoxide Emissions, Geophys. Res. Lett., 44, 9985–9995, https://doi.org/10.1002/2017GL074987, 2017.

Gettelman, A., Mills, M. J., Kinnison, D. E., Garcia, R. R., Smith, A. K., Marsh, D. R., Tilmes, S., Vitt, F., Bardeen, C. G., McInerny, J., Liu, H.-L., Solomon, S. C., Polvani, L. M., Emmons, L. K., Lamarque, J.-F., Richter, J. H., Glanville, A. S., Bacmeister, J. T., Phillips, A. S., Neale, R. B., Simpson, I. R., DuVivier, A. K., Hodzic, A., and Randel, W. J.: The Whole Atmosphere Community Climate Model Version 6 (WACCM6), Journal

of Geophysical Research: Atmospheres, 124, 12380–12403, https://doi.org/10.1029/2019JD030943, 2019.

Hand, J. L., Schichtel, B. A., Malm, W. C., and Frank, N. H.: Spatial and Temporal Trends in $PM_{2.5}$ Organic and Elemental Carbon across the United States, Advances in Meteorology, 2013, e367674, https://doi.org/10.1155/2013/367674, 2013.

He, H., Liang, X.-Z., Sun, C., Tao, Z., and Tong, D. Q.: The long-term trend and production sensitivity change in the US ozone pollution from observations and model simulations, Atmos. Chem. Phys., 20, 3191–3208, https://doi.org/10.5194/acp-20-3191-2020, 2020.

Im, U., Brandt, J., Geels, C., Hansen, K. M., Christensen, J. H., Andersen, M. S., Solazzo, E., Kioutsioukis, I., Alyuz, U., Balzarini, A., Baro, R., Bellasio, R., Bianconi, R., Bieser, J., Colette, A., Curci, G., Farrow, A., Flemming, J., Fraser, A., Jimenez-Guerrero, P., Kitwiroon, N., Liang, C.-K., Nopmongcol, U., Pirovano, G., Pozzoli, L., Prank, M., Rose, R., Sokhi, R., Tuccella, P., Unal, A., Vivanco, M. G., West, J., Yarwood, G., Hogrefe, C., and Galmarini, S.: Assessment and economic valuation of air pollution impacts on human health over Europe and the United States as calculated by a multi-model ensemble in the framework of AQMEII3, Atmospheric Chemistry and Physics, 18, 5967–5989, https://doi.org/10.5194/acp-18-5967-2018, 2018.

Inness, A., Ades, M., Agustí-Panareda, A., Barré, J., Benedictow, A., Blechschmidt, A.-M., Dominguez, J. J., Engelen, R., Eskes, H., Flemming, J., Huijnen, V., Jones, L., Kipling, Z., Massart, S., Parrington, M., Peuch, V.-H., Razinger, M., Remy, S., Schulz, M., and Suttie, M.: The CAMS reanalysis of atmospheric composition, Atmospheric Chem. Phys., 19, 3515–3556, https://doi.org/10.5194/acp-19-3515-2019, 2019.

Jaffe, D. and Ray, J.: Increase in surface ozone at rural sites in the western US, Atmospheric

Environment, 41, 5452–5463, https://doi.org/10.1016/j.atmosenv.2007.02.034, 2007.

Jaffe, D., Price, H., Parrish, D., Goldstein, A., and Harris, J.: Increasing background ozone during spring on the west coast of North America, Geophysical Research Letters, 30, https://doi.org/10.1029/2003GL017024, 2003.

Kong, L., Tang, X., Zhu, J., Wang, Z., Li, J., Wu, H., Wu, Q., Chen, H., Zhu, L., Wang, W., Liu, B., Wang, Q., Chen, D., Pan, Y., Song, T., Li, F., Zheng, H., Jia, G., Lu, M., Wu, L., and Carmichael, G. R.: A 6-year-long (2013–2018) high-resolution air quality reanalysis dataset in China based on the assimilation of surface observations from CNEMC, Earth Syst. Sci. Data, 13, 529–570, https://doi.org/10.5194/essd-13-529-2021, 2021.

Koumoutsaris, S. and Bey, I.: Can a global model reproduce observed trends in summertime surface ozone levels?, Atmospheric Chemistry and Physics, 12, 6983–6998, https://doi.org/10.5194/acp-12-6983-2012, 2012.

Kumar, Rajesh, and He, C. (2023). CONUS air quality reanalysis dataset (2005-2018). Version 1.0. UCAR/NCAR - GDEX. https://doi.org/10.5065/cfya-4g50. Accessed 15 May 2024.

Kumar, R., Monache, L. D., Bresch, J., Saide, P. E., Tang, Y., Liu, Z., Silva, A. M. da, Alessandrini, S., Pfister, G., Edwards, D., Lee, P., and Djalalova, I.: Toward Improving Short-Term Predictions of Fine Particulate Matter Over the United States Via Assimilation of Satellite Aerosol Optical Depth Retrievals, Journal of Geophysical Research: Atmospheres, 124, 2753–2773, https://doi.org/10.1029/2018JD029009, 2019.

Lin, M., Horowitz, L. W., Payton, R., Fiore, A. M., and Tonnesen, G.: US surface ozone trends and extremes from 1980 to 2014: quantifying the roles of rising Asian emissions, domestic controls, wildfires, and climate, Atmos. Chem. Phys., 17, 2943–2970, https://doi.org/10.5194/acp-17-2943-2017, 2017.

Liu, Z., Liu, Q., Lin, H.-C., Schwartz, C. S., Lee, Y.-H., and Wang, T.: Three-dimensional variational assimilation of MODIS aerosol optical depth: Implementation and application to a dust storm over East Asia, Journal of Geophysical Research: Atmospheres, 116, https://doi.org/10.1029/2011JD016159, 2011.

Malm, W. C. and Hand, J. L.: An examination of the physical and optical properties of aerosols collected in the IMPROVE program, Atmospheric Environment, 41, 3407–3427, https://doi.org/10.1016/j.atmosenv.2006.12.012, 2007.

Marsh, D. R., Mills, M. J., Kinnison, D. E., Lamarque, J.-F., Calvo, N., and Polvani, L. M.: Climate Change from 1850 to 2005 Simulated in CESM1(WACCM), J. Climate, 26, 7372–7391, https://doi.org/10.1175/JCLI-D-12-00558.1, 2013.

McClure, C. D. and Jaffe, D.: US particulate matter air quality improves except in wildfire-prone areas, PNAS, 115, 7901–7906, https://doi.org/10.1073/pnas.1804353115, 2018.

Miyazaki, K., Bowman, K., Sekiya, T., Eskes, H., Boersma, F., Worden, H., Livesey, N., Payne, V. H., Sudo, K., Kanaya, Y., Takigawa, M., and Ogochi, K.: Updated tropospheric chemistry reanalysis and emission estimates, TCR-2, for 2005–2018, Earth Syst. Sci. Data, 12, 2223–2259, https://doi.org/10.5194/essd-12-2223-2020, 2020.

Nolte, C. G., Appel, K. W., Kelly, J. T., Bhave, P. V., Fahey, K. M., Collett, J. L. J., Zhang, L., and Young, J. O.: Evaluation of the Community Multiscale Air Quality (CMAQ) model v5.0 against size-resolved measurements of inorganic particle composition across sites in North America, Geoscientific Model Development, 8, 2877–2892, https://doi.org/10.5194/gmd-8-2877-2015, 2015.

Orozco, D., Reeves, U., and Levine, N.: Polluted Parks: How Air Pollution and Climate Change Continue to Harm America's National Parks., National Parks Conservation Association

(NPCA). Washington, DC., 2024.

Pagowski, M., Liu, Z., Grell, G. A., Hu, M., Lin, H.-C., and Schwartz, C. S.: Implementation of aerosol assimilation in Gridpoint Statistical Interpolation (v. 3.2) and WRF-Chem (v. 3.4.1), Geoscientific Model Development, 7, 1621–1627, https://doi.org/10.5194/gmd-7-1621-2014, 2014.

Parrish, D. D., Dunlea, E. J., Atlas, E. L., Schauffler, S., Donnelly, S., Stroud, V., Goldstein, A. H., Millet, D. B., McKay, M., Jaffe, D., Price, H. U., Hess, P. G., Flocke, F., and Roberts, J. M.: Changes in the photochemical environment of the temperate North Pacific troposphere in response to increased Asian emissions, Journal of Geophysical Research: Atmospheres, 109, https://doi.org/10.1029/2004JD004978, 2004.

Parrish, D. D., Millet, D. B., and Goldstein, A. H.: Increasing ozone in marine boundary layer inflow at the west coasts of North America and Europe, Atmospheric Chemistry and Physics, 9, 1303–1323, https://doi.org/10.5194/acp-9-1303-2009, 2009.

Pozzoli, L., Janssens-Maenhout, G., Diehl, T., Bey, I., Schultz, M. G., Feichter, J., Vignati, E., and Dentener, F.: Re-analysis of tropospheric sulfate aerosol and ozone for the period 1980–2005 using the aerosol-chemistry-climate model ECHAM5-HAMMOZ, Atmospheric Chemistry and Physics, 11, 9563–9594, https://doi.org/10.5194/acp-11-9563-2011, 2011.

Remer, L. A., Kaufman, Y. J., Tanré, D., Mattoo, S., Chu, D. A., Martins, J. V., Li, R.-R., Ichoku, C., Levy, R. C., Kleidman, R. G., Eck, T. F., Vermote, E., and Holben, B. N.: The MODIS Aerosol Algorithm, Products, and Validation, J. Atmos. Sci., 62, 947–973, https://doi.org/10.1175/JAS3385.1, 2005.

Saide, P. E., Carmichael, G. R., Liu, Z., Schwartz, C. S., Lin, H. C., da Silva, A. M., and Hyer,

E.: Aerosol optical depth assimilation for a size-resolved sectional model: impacts of observationally constrained, multi-wavelength and fine mode retrievals on regional scale analyses and forecasts, Atmospheric Chemistry and Physics, 13, 10425–10444, https://doi.org/10.5194/acp-13-10425-2013, 2013.

Seyedali Mousavinezhad, Masoud Ghahremanloo, Yunsoo Choi, Arman Pouyaei, Nima Khorshidian, Bavand Sadeghi, Surface ozone trends and related mortality across the climate regions of the contiguous United States during the most recent climate period, 1991–2020,

Simon, H., Reff, A., Wells, B., Xing, J., and Frank, N.: Ozone Trends Across the United States over a Period of Decreasing NOx and VOC Emissions, Environ. Sci. Technol., 49, 186–195, https://doi.org/10.1021/es504514z, 2015.

Strode, S. A., Rodriguez, J. M., Logan, J. A., Cooper, O. R., Witte, J. C., Lamsal, L. N., Damon, M., Van Aartsen, B., Steenrod, S. D., and Strahan, S. E.: Trends and variability in surface ozone over the United States, Journal of Geophysical Research: Atmospheres, 120, 9020–9042, https://doi.org/10.1002/2014JD022784, 2015.

WHO: Billions of people still breathe unhealthy air: new WHO data: https://www.who.int/news/item/04-04-2022-billions-of-people-still-breathe-unhealthy-air-new-who-data, last access: 12 May 2024, 2023.

WHO: https://www.who.int/westernpacific/health-topics/air-pollution , last access: 12 May 2024, 2020.

Wiedinmyer, C., Kimura, Y., McDonald-Buller, E. C., Emmons, L. K., Buchholz, R. R., Tang, W., Seto, K., Joseph, M. B., Barsanti, K. C., Carlton, A. G., and Yokelson, R.: The Fire Inventory from NCAR version 2.5: an updated global fire emissions model for climate

and chemistry applications, EGUsphere, 1–45, https://doi.org/10.5194/egusphere-2023-124, 2023.

Xie, Y., Lin, M., & Horowitz, L. W.: Summer PM2.5 pollution extremes caused by wildfires over the western United States during 2017–2018. Geophysical Research Letters, 47, e2020GL089429. https://doi.org/10.1029/2020GL089429, 2020.

Xing, J., Mathur, R., Pleim, J., Hogrefe, C., Gan, C.-M., Wong, D. C., Wei, C., Gilliam, R., and Pouliot, G.: Observations and modeling of air quality trends over 1990–2010 across the Northern Hemisphere: China, the United States and Europe, Atmospheric Chemistry and Physics, 15, 2723–2747, https://doi.org/10.5194/acp-15-2723-2015, 2015.

Zhang, Y., West, J. J., Mathur, R., Xing, J., Hogrefe, C., Roselle, S. J., Bash, J. O., Pleim, J. E., Gan, C.-M., and Wong, D. C.: Long-term trends in the ambient $PM_{2.5}$- and O_3-related mortality burdens in the United States under emission reductions from 1990 to 2010, Atmospheric Chemistry and Physics, 18, 15003–15016, https://doi.org/10.5194/acp-18-15003-2018, 2018.